Universität Bonn

Physikalisches Institut

Studies of a top quark mass measurement in the dilepton channel using the m_{T2} variable at ATLAS

Kaven Yau Wong

A measurement of the top quark mass in the dilepton channel is studied. A mass measurement in the dilepton channel is challenging, due to the production of two neutrinos. In order to circumvent this difficulty, the m_{T2} variable is used. The m_{T2} variable is used in pair production events with two missing particles and represents a lower bound to the parent particles mass.

The mass measurement is based on the calibration curve method, with pp collision data at the LHC, measured with the ATLAS detector. Applying this method on 2 fb^{-1} ATLAS data, a measurement of the top mass was made, giving a value of $172.7 \pm 1.4^{+4.2}_{-4.6}$ GeV. This measurement is dominated by the systematic uncertainty, with the jet energy scale systematic uncertainty giving the strongest contribution. The jet energy scale systematic uncertainty was reduced by combining the mass measurement using m_{T2} with a mass measurement performed with p_T^{leptons}. An improvement in the value of the systematic uncertainty is achieved with this measurement combination, yielding a top quark mass value of $172.9 \pm 1.2^{+3.4}_{-4.0}$ GeV.

Physikalisches Institut der
Universität Bonn
Nußallee 12
D-53115 Bonn

BONN-IB-2012-03
Januar 2012

Universität Bonn
Physikalisches Institut

Studies of a top quark mass measurement in the dilepton channel using the m_{T2} variable at ATLAS

Kaven Yau Wong

Dieser Forschungsbericht wurde als Masterarbeit von der Mathematisch-Naturwissenschaftlichen Fakultät der Universität Bonn angenommen.

Angenommen am:	12.12.2011
Referent:	Prof. Dr. Norbert Wermes
Koreferentin:	Prof. Dr. Ian Brock

Acknowledgements

I would like to thank Dr. Markus Cristinziani for accepting to be the supervisor of my thesis, as well as for all his help, support, and patience during the development of this thesis project. I would also like to express my gratitude to Prof. Norbert Wermes for accepting to be the referent for this thesis.

I feel much obliged to the DAAD-IFARHU/SENACYT scholarship program, the Bonn-Cologne Graduate School Honors Programme, and the Physikalisches Institut (Bonn University) for their financial support.

Furthermore, I would like show my appreciation to Dr. Kirika Uchida for her invaluable help during this year; to Agnieszka Leyko for helping in the editing of this thesis; and to my partner Elisavet Proedrou for helping in the editing and proofreading of my thesis, as well as for her unconditional love, support, and understanding during this time.

Finally, I would like to thank my father, my mother, and my sister for all the moral, emotional, and financial support offered during all my life, specially during the almost three years that I have been far from home.

Contents

Introduction

The standard model of particle physics is an attempt to answer one of the ancient questions of humankind: what are the basic components of matter?

In the standard model, matter is composed of quarks, leptons, and bosons. The top quark is part of the standard model of Particle Physics. It was predicted by Kobayashi and Maskawa in 1973 [20] and discovered by the CDF collaboration in 1995 [5]. The top quark is the heaviest known elementary particle in the standard model, with a measured mass of $m_{top} = 173.2 \pm 0.9$ GeV according to the latest Tevatron measurement [36].

The value of the top quark mass is an unkown parameter of the standard model, i.e. it cannot be obtained by theoretical calculations. As the heaviest elementary particle in the standard model, the top quark produces a significant contribution to the electroweak radiative corrections. A precise measurement set constrains on the hypothetical Higgs boson mass, as well as other particles predicted by physics models beyond the standard model [31].

The objective of this thesis is to measure the top quark mass in the dilepton channel, using data provided by LHC and the ATLAS detector. The method used is based on the m_{T2} variable (also known as the stransverse mass) [8]. The m_{T2} variable is used mainly in exotic particle searches in pair production events with two undetected particles and represents a lower bound to the parent particle mass. A $t\bar{t}$ event decaying through the dilepton channel would have the same signature, as each parent particle decays into a b-jet, a lepton, and a neutrino. Therefore, the m_{T2} variable can be used in this decay channel.

The first chapter of this thesis is the theoretical background. At first, an introduction to the standard model is given. Afterwards, the properties of the top quark are discussed in some details, including the top dilepton decay channel. At the end of the first chapter, a discussion of the m_{T2} variable, the p_T^{leptons} variable, and data combination is presented.

The second chapter is devoted to the LHC and the ATLAS detector. A general description of the LHC and the ATLAS detector can be found here.

The methodology is found in the third chapter. First, a description of the method used to measure the top quark mass is given. Afterwards, the event selection is discussed. Finally, more technical details about the computation of m_{T2}, the computer tools used, the samples used, and the process used to obtain the m_{T2} and p_T^{leptons} distributions and calibration curves is shown.

Chapter four contains a discussion about the systematic uncertainties that affects the mass measurement.

Finally, the analysis and results can be found in the fifth chapter. It contains many histograms and plots that were produced using the methodology described in the former chapters. From the analysis of these plots, the top quark mass is measured, as well as the uncertainty in its computation.

The last chapter contains the conclusions and recommendations. It summarizes the thesis' main results and points out possible ways to improve these results.

Chapter 1

Theoretical background

1.1 The standard model of particle physics

This section is a compact summary of the standard model based on the information found in [15, 30].

The standard model is a theory of particles and their interactions. As a theory of particles, the standard model states that all matter is composed of elemental spin $\frac{1}{2}$ particles (fermions): quarks and leptons. Each of these particles has its own antiparticle, which has the same mass but opposite charge [1].

As a theory of fundamental interactions, the standard model is a perturbative quantum field theory; i.e., interactions are understood as an exchange of mediator particles. The mediators in standard model are integer spin particles (bosons). These mediators can be split in three groups, which correspond to the three interactions that standard model considers: strong, weak, and electromagnetic.

The standard model is considered an incomplete theory of fundamental interactions, as it does not consider one of the four fundamental interactions: gravity. Nevertheless, this does not stop it from being a very successful theory, as the contribution of gravity is negligible at the current energy scale used in particle physics.

1.1.1 Leptons

There are six leptons in the standard model, divided in three generations. Each generation is composed of a negatively charged lepton, and a neutrally charged neutrino named after its corresponding charged lepton. The names and symbol are shown in Table 1.1.

Generation	Charged lepton			Neutrino	
	Name	Symbol	Mass	Name	Symbol
First	electron	e	511.0 keV	electron neutrino	ν_e
Second	muon	μ	105.7 MeV	muon neutrino	ν_μ
Third	tau	τ	1.777 GeV	tau neutrino	ν_τ

Table 1.1: Lepton names and their respective symbols

The leptons are particles that are not affected by the strong interaction, but are affected by the other interactions. All leptons can be found as isolated particles.

All negatively charged leptons have the same charge (-1), but different masses[2]. The neutrinos are very difficult to detect: they are stable, neutral, and almost massless particles($m_\nu < 2$ eV); therefore, neutrino detection must rely mainly on weak interaction processes.

---

[1] In this thesis, the term *charge* is to be understood as *electrical charge*.

[2] Lepton anti-particles have charge $+1$

1.1.2 Quarks

There are also six quarks in the standard model divided in three generations. Each generation has one particle with charge $+\frac{2}{3}$ and one particle with charge $-\frac{1}{3}$. The names and symbol are shown in Table 1.2.

Generation	Charge $+\frac{2}{3}$			Charge $-\frac{1}{3}$		
	Name	Symbol	Mass	Name	Symbol	Mass
First	up	u	1.7 – 3.3 MeV	down	d	4.1 – 5.8 MeV
Second	charm	c	1.3 GeV	strange	s	101 MeV
Third	top/truth	t	173.2 GeV	bottom/beauty	b	4.2 GeV

Table 1.2: quarks names and their respective symbols

Unlike leptons, quarks are affected by the strong interaction, as well as the other interactions. Furthermore, the charge is not an integer multiple of the electron charge, and no isolated quark has been observed.

1.1.3 Mediators

The standard model considers that any fundamental interaction between two particles is done by the exchange of a mediator. Each interaction has different mediators, as shown in Table 1.3.

Interaction	mediators names	symbol	Charge	Mass
Electromagnetic	photon	γ	0	0
Weak	W^+ boson	W^+	+1	80.4 GeV
	W^- boson	W^-	−1	80.4 GeV
	Z^0 boson	Z^0	0	91.2 GeV
Strong	gluon (8 types)	g	0	0

Table 1.3: mediators in the standard model

The electromagnetic interaction is probably the most known fundamental interaction. It is responsible for the interaction between electrical charges, and keeps the electrons around the nucleus. An example of an electromagnetic interaction is shown in Figure 1.1a.

The weak interaction is responsible for various decays, particularly the beta decay, where a neutron decays into a proton, a lepton and its corresponding antineutrino (See Figure 1.1b). This interaction allows quarks to decay into a lighter quark and leptons, a phenomenon that could not be explained without the existence of the weak interaction.

The strong interaction is the force responsible for holding the nucleus together. The physical theory that studies the strong interaction is called chromodynamics. In addition to the electric charge, there is a "color charge" that acts at short distances. This interaction affects only quarks (and other gluons) and keeps them confined. The existence of this interaction is used to explain why quarks hadronize, and why a single isolated quark cannot be found. Figure 1.1c shows the process of gluon fusion and further decay to a $t\bar{t}$ pair.

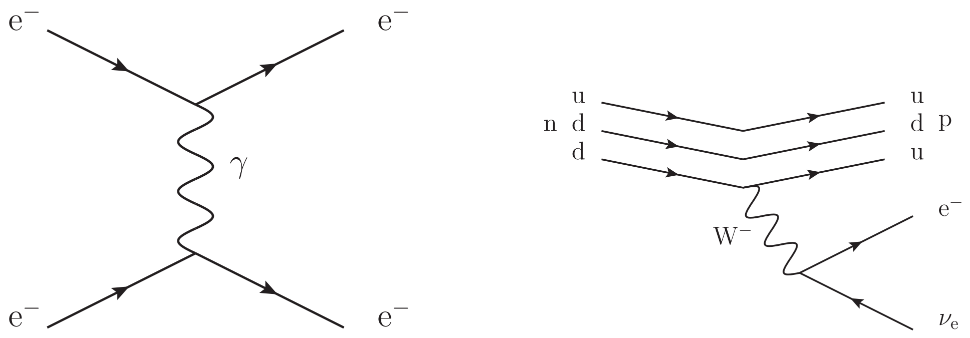

(a) Electron-electron scattering (t-channel)

(b) Beta decay

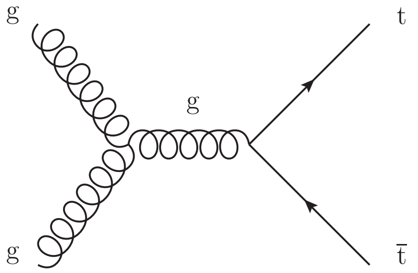

(c) Gluon fusion with $\mathrm{t\bar{t}}$ pair production

Figure 1.1: Examples of interactions studied in the standard model

1.2 The top quark

The top quark is the heaviest known elementary particle in the standard model. The world's best measurement of its mass is provided by the Tevatron. The latest Tevatron measurement assigns to the top quark a mass of m_{top} = 173.2 ± 0.6(stat) ± 0.8(syst) GeV using 5.8 fb^{-1} of data [36].

Due to its huge mass, its lifetime is very short, of the order of 10^{-24} s [32]. This has two consequences:

- The top quark decays before it can be detected.
- The top quark decays before it can hadronize [29].

The first consequence means that instead of direct detection, its production has to be inferred from its decay products.

In order to understand the second consequence, it is good to revise the concept of hadronization. When a free quark or gluon is produced, it does not remain free due to color confinement. Instead, it combines with quark antiquark pairs produced from the vacuum, producing hadrons. This process is called hadronization. Hadronization produces highly collimated jets formed by many particles. As the top quark decays before it can hadronize, $\mathrm{t\bar{t}}$ events have a characteristic signature, which helps in the candidate selection process. This also also allow us to measure its charge, spin, polarization, and other observables that cannot be measured easily in other quarks.

The top quark decays 99^{+9}_{-8} % to a W boson and a bottom quark. The bottom quark usually hadronizes and forms a b-jet, while the W boson decays hadronically (68%) and or leptonically (32%) [16].

Therefore, for a $\mathrm{t\bar{t}}$ pair production, the $\mathrm{t\bar{t}}$ pair decays mainly in three channels, depending on how the W boson decays. This is shown in Table 1.4.

Decay channel	W decays	Jets	Leptons	Probability
Full hadronic	Both hadronically	4	0	0.46
Semileptonic	One hadronically and one leptonically	3	1	0.44
Dileptonic	Both leptonically	2	2	0.10

Table 1.4: $t\bar{t}$ decay channels

Note that in an experiment, the number of jets and leptons shown in Table 1.4 is modified by other physical processes, such as the initial state radiation, the final state radiation, pile-up effects, etc.

As this study describes a measurement of the top quark mass, it is interesting to show the results obtained from other ATLAS studies, as well as other experiments like CMS, CDF, and D0. A summary is shown in Table 1.5.

Experiment	CDF and D0 [36]	CMS [11]	ATLAS [23]	ATLAS [24]
Collision particles	proton-antiproton	proton-proton	proton-proton	proton-proton
Channel	Many, combined	Dilepton	Lepton+jets	Lepton+jets
Center-of-mass Energy	1.96 TeV	7 TeV	7 TeV	7 TeV
Luminosity	5.8 fb^{-1}	36 pb^{-1}	35 pb^{-1}	0.70 fb^{-1}
Mass measurement	173.2 GeV	175.5 GeV	166.4 GeV	175.9 GeV
Statistical uncertainty	0.6 GeV	4.6 GeV	4.0 GeV	0.9 GeV
Systematic uncertainty	0.8 GeV	4.6 GeV	4.9 GeV	2.7 GeV

Table 1.5: Different top quark mass measurements

1.2.1 The dilepton channel

The top dilepton channel is defined as follows: given a $t\bar{t}$ pair production, each t quark decays into a W boson and a bottom quark. The bottom quarks form two b-jets, while the W bosons decay leptonically. This situation is depicted in Figure 1.2.

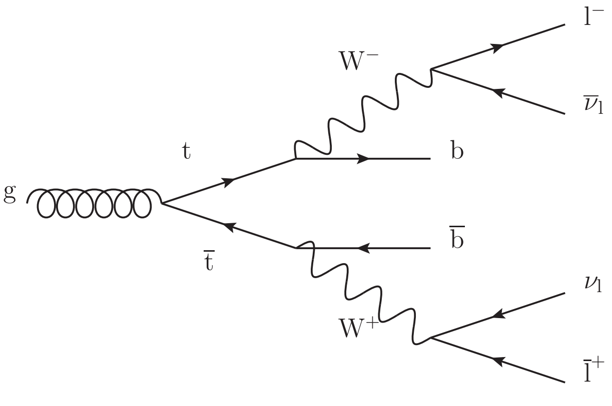

Figure 1.2: Feynman diagram for the top dilepton channel

For decays into electrons or muons, the events give a clear signature: two leptons, two jets, and missing transverse momentum[3].

If the W decays into a tau, the situation is different. Due to the high mass of the tau, the tau has a very short lifetime, and therefore it decays before it can be directly observed. The tau decays most of the times hadronically (65%). But when they decay leptonically(35%), the final signature looks the same as the decay into electrons or muons. There is no way to determine whether the electron or muon comes directly from the W boson decay or from a tau decay.

Therefore, depending on the final signature, the top dilepton channel is subdivided into three decay modes, shown in Table 1.6.

Decay mode	Symbol	Final signature
electron-electron	ee	two electrons, two jets, missing transverse momentum
electron-muon	eμ	one electron, one muon, two jets, missing transverse momentum
muon-muon	$\mu\mu$	two muons, two jets, missing transverse momentum

Table 1.6: Top dilepton channel decay modes

Note that in all cases, the electrons or the muons could have been actually produced by a tau decay, rather than from a W decay.

1.3 The m_{T2} variable

The m_{T2} variable, also known as the stransverse mass, is a kinematic variable used in pair-production events where each parent particle decays into visible particles and one undetected (invisible) particle [22, 8]. The top dilepton channel is an example of such a decay (See Figure 1.2).

The motivation to use the m_{T2} variable to measure the top quark mass is the fact that m_{T2} depends on the parent particle mass. As a matter of fact, it represents a lower boundary to the parent particle mass. The proofs and further discussions on this property can be found in [8, 12].

Formally, the m_{T2} variable can be defined as follows [3]:

$$m_{T2}(m_{invis}) = \min_{\vec{p}_T^{(1)},\,\vec{p}_T^{(2)}} \Big[\max\big[m_T(m_{invis}, \vec{p}_T^{(1)}), m_T(m_{invis}, \vec{p}_T^{(2)})\big]\Big] \tag{1.3.1}$$

where

$$\vec{p}_T^{(1)} + \vec{p}_T^{(2)} = \vec{p}_T^{\text{miss}} \tag{1.3.2}$$

$$m_T(m_{invis}, \vec{p}_T^{(n)}) = \sqrt{m_{vis}^2 + m_{invis}^2 + 2(E_T^{vis} E_T^{invis} - \vec{p}_T^{vis} \cdot \vec{p}_T^{(n)})} \tag{1.3.3}$$

such that all the visible and invisible particles in Eq. 1.3.3 come from the same parent particle.

Here, E_T is the transverse energy[4], m is the mass, $\vec{p}_T$ is the transverse momentum, and $\vec{p}_T^{\text{miss}}$ is the missing transverse momentum; vis represents the sum of all detected particles in each decay, and $invis$ stands for the undetected particle in each decay.

The definition might seem a little confusing and complicated at first sight, but its meaning and motivation will soon become clear, as we apply the m_{T2} variable on the top dilepton channel.

---

[3] Defined in appendix A

[4] Defined in appendix A

1.3.1 The m_{T2} variable in the top dilepton channel

As mentioned in Subsection 1.2.1, the top dilepton channel signature is two leptons, two jets and missing transverse momentum, where each parent particle produces one lepton (visible), one jet(visible) and one neutrino(invisible). In this situation, the m_{T2} variable can be used.

When only one neutrino is produced, its transverse momentum can be associated with $\vec{p}_T^{\,\text{miss}}$. But when two or more neutrinos are present, the invisible particles transverse momentum cannot be inferred from $\vec{p}_T^{\,\text{miss}}$ individually. In this case, $\vec{p}_T^{\,\text{miss}}$ is associated with the vectorial sum of the transverse momentum of all invisible particles. For the dilepton channel, this requirement is set with the constrain shown in Eq. 1.3.2, where the superscripted number identifies which neutrino is considered. For the sake of argumentation, let us consider the first one coming from the top quark, and the second one coming from the antitop quark.

Considering the neutrinos mass negligible, the invisible mass term in Eq. 1.3.3 is zero. Furthermore,

$$E_T^{invis} = \|\vec{p}_T^{\,invis}\| \tag{1.3.4}$$

The values tagged with vis can be deduced from the visible particles four-momentum, defined as:

$$P_{vis}^{(n)} = P_{\text{lepton}}^{(n)} + P_{\text{b-jet}}^{(n)} \tag{1.3.5}$$

For the invisible particles, things are not that straightforward. As stated before, the values for $\vec{p}_T^{\,(n)}$ cannot be measured directly. Instead, their values are asigned according to Eq. 1.3.1 subject to the constrain given by Eq. 1.3.2.

In order to understand Eq. 1.3.1, a more detailed discussion on its components is needed. Eq. 1.3.1 states that the m_{T2} variable is the minimum value of the maximum between two m_T distributions. Figure 1.3 shows how m_T behaves with $\vec{p}_T^{\,(n)}$. In the dilepton channel, the invisible particles are neutrinos, and we can consider $\vec{p}_T^{\,(1)} = \vec{p}_T^{\,\nu}$. For two given m_T distributions, they can either intersect or not intersect.

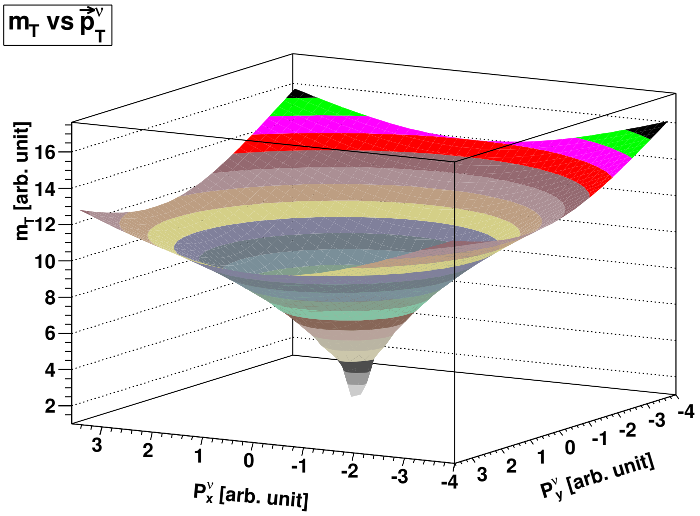

Figure 1.3: m_T distribution

- If they do not intersect (Figure 1.4a), the maximum between the two m_T distributions is the same as the m_T distribution that has the higher m_T value at every point (colored surface).

- If they do intersect (Figure 1.4b). the maximum between the two m_T distribution is a surface formed by the points with the higher m_T value.

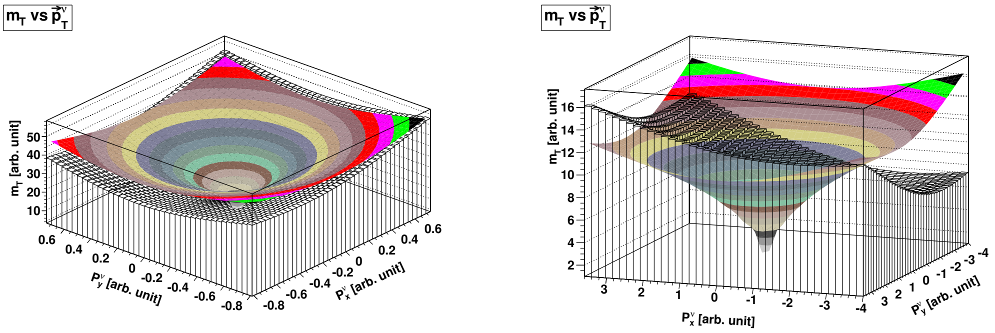

(a) m_T distributions without intersect

(b) m_T distributions with intersect

Figure 1.4: m_T distribution possible configurations

Given the solution surface for the maximum between two m_T distributions, the m_{T2} value is given by the minimum m_T value on this solution surface.

Note that $\vec{p}_T^{(1)}$ and $\vec{p}_T^{(2)}$ are not independent. Therefore, the minimization is made varying one of them and using Eq. 1.3.2 to obtain the other. This means that the two m_T values in Eq. 1.3.1 can be obtained as a function of $\vec{p}_T^{(1)}$ (or $\vec{p}_T^{(2)}$).

If the mass of the invisible particle is unknown, a trial mass value is used. An interesting feature of m_{T2} arises in this case, as the m_{T2} distribution on this trial mass shows a kink structure when the trial mass value is close to the invisible particle's real mass value.

1.4 Leptons transverse momentum norm

The norm of the transverse momentum of the leptons in the dilepton channel is defined as the norm of the vectorial sum of the transverse momentum of each lepton taking place in the event. That is:

$$p_T^{\text{leptons}} = \|\vec{p}_T^{(\text{lep1})} + \vec{p}_T^{(\text{lep2})}\| \tag{1.4.1}$$

The dependence of this quantity with the particle's top mass is obvious: when a particle decays, its energy is used to produce the new particles and their momenta. If the number of particles produced is fixed (by choosing a given channel), then a more massive particle would produce particles with higher momenta, and, in this particular case, the leptons would have in average a higher transverse momentum.

The dependency of p_T^{leptons} with the parent mass makes it useful as a second top mass measurement. As it will be seen later, this variable is used to improve the top quark mass measurement made with the m_{T2} variable by means of a measurement combination[5].

---

[5] See appendix B

Chapter 2

Experimental setup

2.1 The LHC accelerator

LHC is the acronym for Large Hadron Collider, a circular superconducting accelerator located in the border between France and Switzerland, close to the city of Geneva, Switzerland (See Figure 2.1).

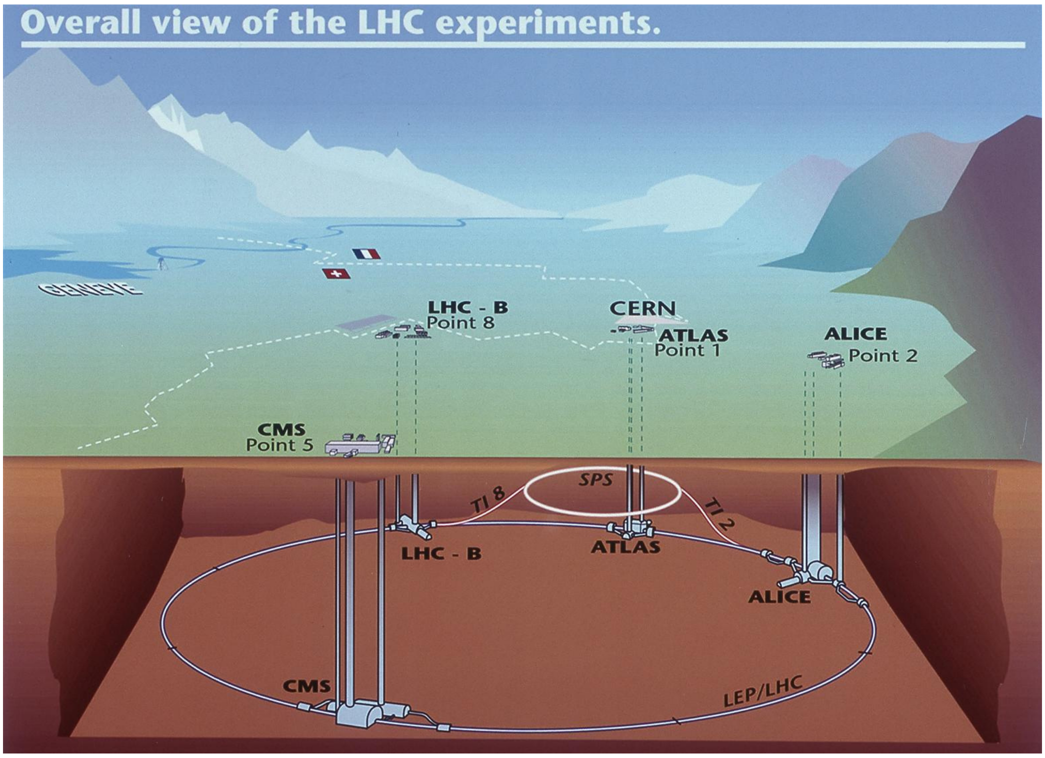

Figure 2.1: LHC location and overall layout(©2011 CERN)

The LHC is designed as a proton-proton collider. Each proton beam contains up to 2808 bunches, where each bunch contains 1.15×10^{11} protons. The protons in each bunch can be accelerated up to 7 GeV, giving a total of 14 TeV center of mass energy. These bunches are brought into collision in four collision points.

The protons are accelerated in a series of steps (For spatial reference, see Figure 2.2):

1. The protons are produced from a hydrogen source and accelerated to an energy of 5 MeV using the Linear Accelerator (LINAC).

2. These protons are sent to the Synchrotron Booster (BOOSTER) where they acquire an energy of 1.4 GeV.
3. The Proton Synchrotron (PS) accelerates them to an energy of 25 GeV.
4. To further increase the energy, the protons are accelerated in the Super Proton Synchrotron (SPS), up to 450 GeV.
5. The protons are sent to the LHC ring, where radio frequency (RF) cavities accelerates the protons up to 7 TeV.

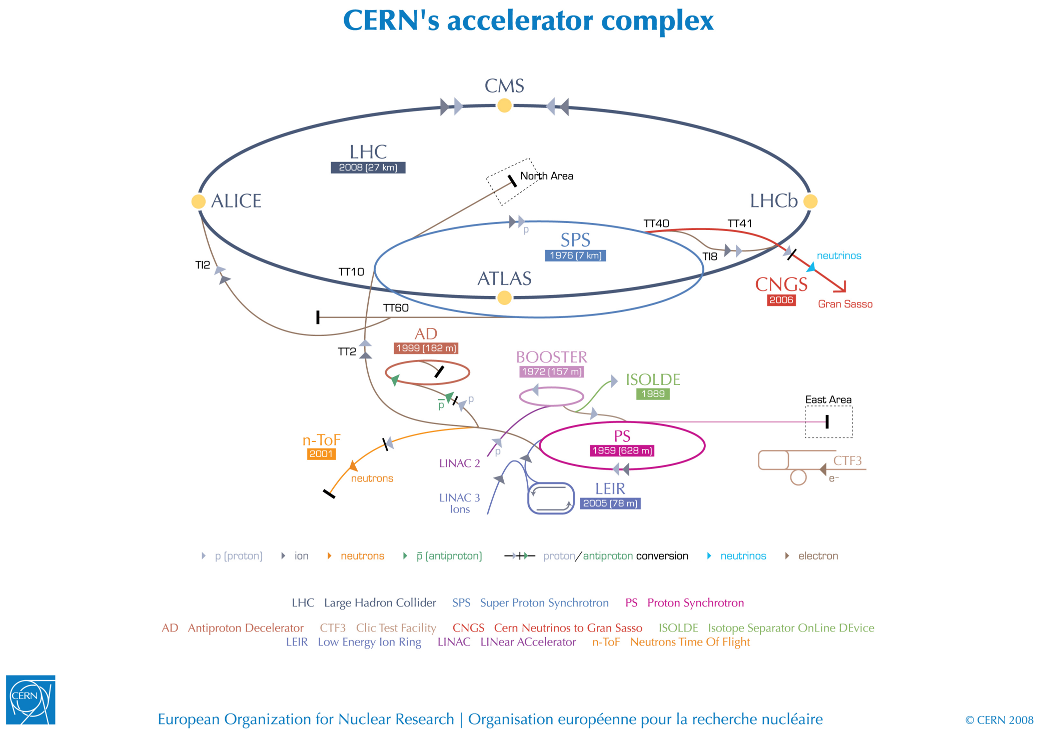

Figure 2.2: Schematic view of CERN's accelerator complex (©2011 CERN)

Currently, the LHC is running at half its designed beam energy (3.5 GeV each beam, for a total of 7 GeV center of mass energy), but it will eventually reach its designed energy after the technical stop taking place on 2012. For complete details about the LHC, please read [9].

The LHC is considered a top quark factory, producing $t\bar{t}$ pairs mainly by gluon fusion (See Figure 2.3). The gluons participating in the fusion are provided by the two colliding protons.

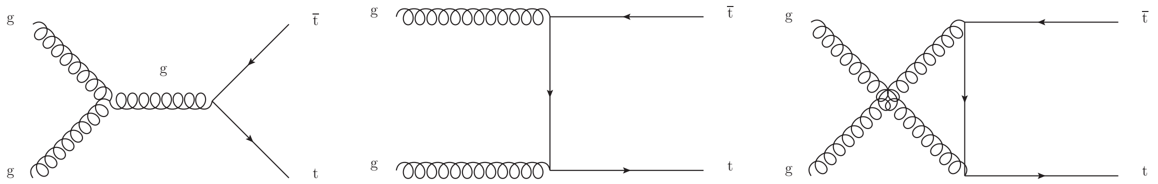

Figure 2.3: Gluon fusion leading order Feynman diagrams

The 27 km long storage ring houses the LHC four main experiments: ATLAS, CMS, ALICE, and LHCb (See Figure 2.2. Each one of those experiments are located in one of the four collision points. ATLAS and CMS are general-purpose detectors, while ALICE is a heavy-ion detector [4], and LHCb is devoted to precision measurements of CP violation and rare decays of B hadrons [7].

2.2 The ATLAS detector

This thesis uses data collected by the ATLAS detector (See Figure 2.4). ATLAS stands for *A Toroidal LHC ApparatuS*, and it is a general-purpose detector for the LHC, designed to accomodate a wide range of studies. It consists of four main components: the inner detector, the electromagnetic calorimeter, the hadron calorimeter, and the muon spectrometer [2]. These provide information used for vertex location, particle charge determination, jet reconstruction, $\vec{p}_T^{\text{miss}}$ determination, energy and momentum measurement, and so on. Additionally to these four components, the trigger system decides which events are to be recorded.

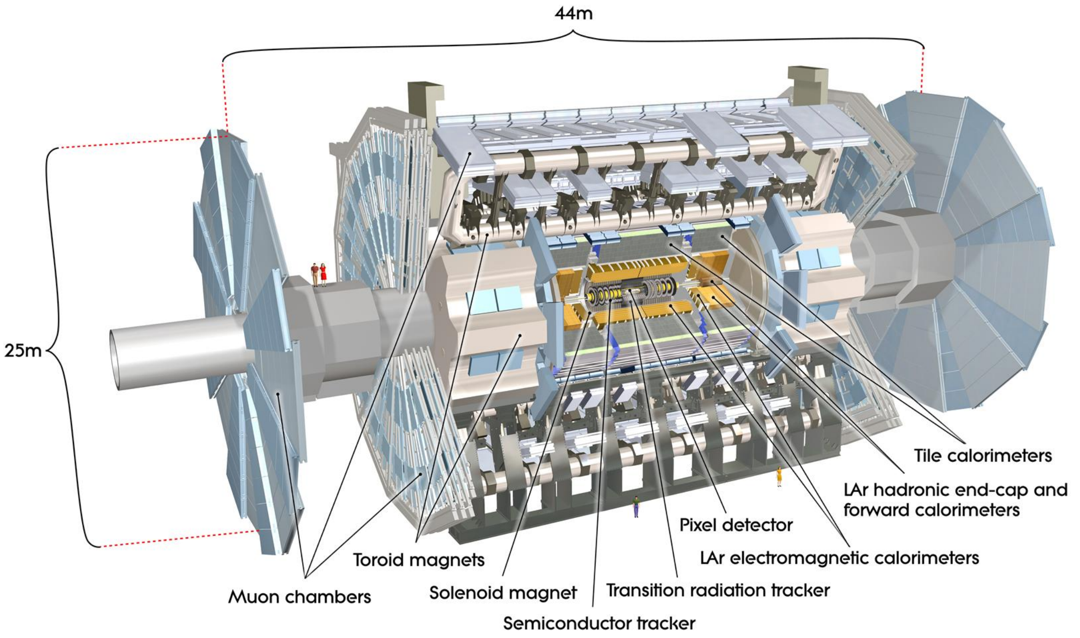

Figure 2.4: Overview of the ATLAS detector

In the following subsections, a brief description of the main components of ATLAS is given. For a complete description of the detector, please refer to [1].

2.2.1 The inner detector

The inner detector provides information that allow the measurement of the momentum and charge of each charged particle. It is located inside the central solenoid, which provides a 2 T magnetic field.

In order to achieve the high resolution needed for precision measurements, fine-granularity detectors are needed. The highest granularity is obtained using pixel detectors. Nevertheless, the number of pixel detectors introduced is limited, due to the material they introduce in the system as well as the high cost

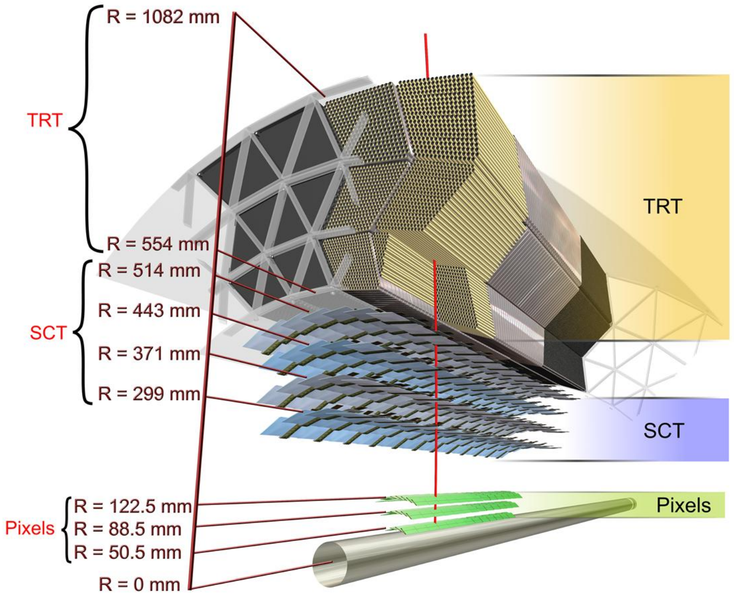

Figure 2.5: ATLAS Inner detector layout(ATLAS Experiment ©2011 CERN)

involved in their production. Therefore, the system consists only of 3 barrels and 5 end-caps disks on each side covering the whole region with $|\eta| < 2.5$.

These three barrels and five disks are formed by approximately 1500 barrel modules and 700 disk modules. Each pixel module is 62.4 mm long and 21.4 mm wide, and contains 46 080 pixel elements with 16 readout chips.

The semiconductor tracker system (SCT) is located behind the pixel detectors. The SCT barrel is formed by eight silicon microstrip detectors layers. Each silicon detector is 64.0 mm long and 63.6 mm wide, containing 768 readout strips. The SCT system contains a surface of 61 m^2, covered by silicon detectors, with 6.2 million readout channels. The system consists of 4 barrel layers and 9 end-cap wheels on each side, the former providing coverage for $|\eta| < 1.4$, and the later providing coverage for $1.4 < |\eta| < 2.5$.

Both the SCT and the pixel system require very high dimensional and thermal stability. This requirement is fulfilled by using materials with low thermal expansion coefficient, as well as a carefully designed cooling system.

The transition radiation tracker (TRT) is the outermost layer in the inner detector. It provides more tracking capabilities, as well as electron identification, providing further discrimination between electrons and hadrons. The system is designed to be able to withstand high hit rates and a good performance in pattern recognition is also achieved.

The barrel module is built with modules containing between 329 and 793 axial straws each, where each straw has a diameter of 4 mm. This barrel covers the $|\eta| < 0.7$ region. The two end-caps are formed by 18 wheels each, and covers the area corresponding to $0.7 < |\eta| < 2.5$.

Figure 2.5 shows the spatial layout of these three systems.

2.2.2 Calorimeters

The ATLAS calorimeters are responsible of measuring the energy of the particles. Calorimetric methods imply the total absorption of the particle energy in a bulk of materials, followed by the measurement of the total energy deposition. Figure 2.6 shows the layout of the calorimeters in ATLAS.

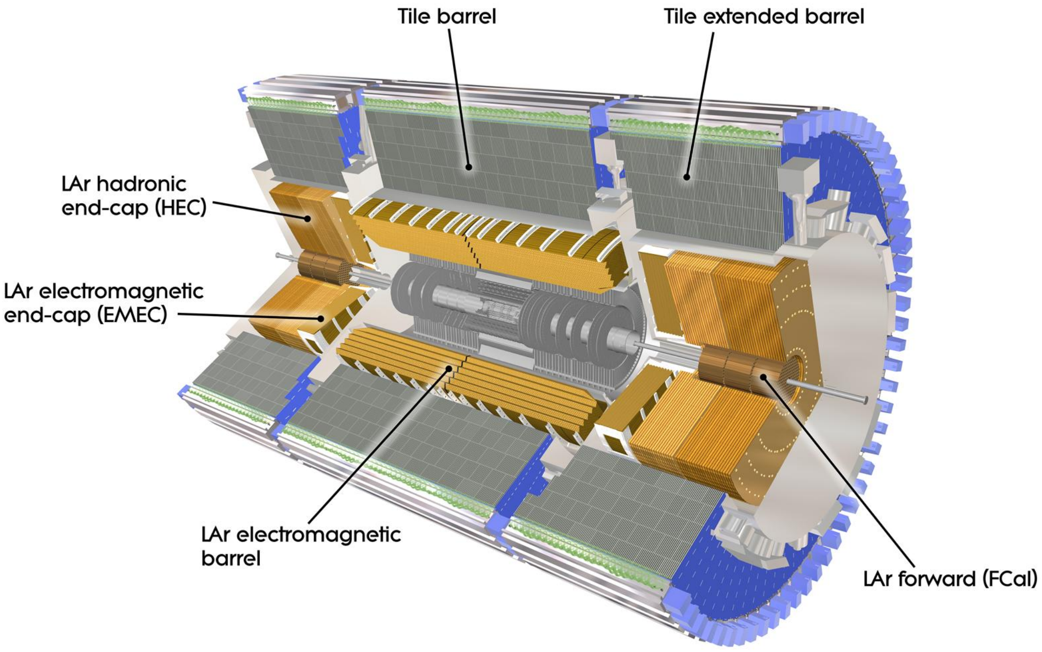

Figure 2.6: ATLAS calorimeter layout (ATLAS Experiment ©2011 CERN)

Electromagnetic calorimeter

At high energies ($E > 100$ MeV), electrons lose their energy almost exclusively by bremsstrahlung radiation, while photons lose their energy in electron-positron pair production. These two processes feed each other, producing electron-photon cascades, which are fundamental in electromagnetic calorimeters functioning. The length scale of a shower is set by the radiation length, which depends on the calorimeter material.

By measuring this cascade, the particle's energy can be determined. This measurement is done by interleaved active material. When the cascade's electrons and protons go through the active material, the material gets ionized. The level of ionization is then measured by collecting the charged particles on electrodes.

The ATLAS electromagnetic calorimeter (EMCal) is a lead/liquid argon (LAr) detector with accordion geometry. The lead plates are used as absorber, while the LAr is used as the active medium.

The EMCal is divided into a barrel part and two end-caps part. The barrel part covers the region corresponding to $|\eta| < 1.475$, while the end-caps covers the region corresponding to $1.375 < |\eta| < 3.2$. The barrel is formed by two identical half-barrels, separated by a 6 mm gap. Each end-cap is divided into two coaxial wheels, covering the regions given by $1.375 < |\eta| < 2.5$ and $2.5 < |\eta| < 3.2$ respectively.

Hadron calorimeter

The hadron calorimeters works with the same principle as electromagnetic calorimeters, but the longitudinal development is determined by the average nuclear interaction length. The average nuclear interaction length is much larger than the average radiation length; therefore, hadron calorimeters need to be much larger than their electromagnetic counterparts.

When designing a hadron calorimeter, its thickness has to be considered, as it has to provide good containment of hadronic showers and reduce punch-through into the next system.

The ATLAS hadron calorimeter is formed by three main components. A scintillating tile calorimeter is used in the barrel region, that is $|\eta| < 1.7$. The hadron end-cap LAr calorimeter (HEC) covers the region $1.5 < |\eta| < 3.2$ Finally, the forward calorimeter (FCal) covers the range $3.1 < |\eta| < 4.1$.

The barrel region is subdivided in two regions: the barrel ($|\eta| < 1.0$) and two extended barrels ($0.8 < |\eta| < 1.7$). All three use iron as the absorber and scintillating tiles as the active material.

Each HEC consists of two independent wheels. The wheel which is closest to the interaction point is made of 25 mm thick copper plates, while the other wheel is made of 50 mm thick copper plates. Each wheel has 32 identical modules.

The FCal is designed to withstand a very high level of radiation. It consist of three sections: one made of copper, and two made of tungsten. In each section, a metal matrix with regularly spaced longitudinal channels is found. The inside of these channels is filled with concentric rods and tubes, and the space between the rods and the tubes is filled with LAr, which is used as the sensitive medium.

2.2.3 Muon spectrometer

Muons are particles that easily go through the calorimeters. Therefore, a system that detects and measures muons is needed: the muon spectrometer.

The ATLAS muon spectrometer is located after both calorimeters, and its operation is based on the deflection of muons using a magnetic field. By combining the signal from the spectrometer with the signal from the tracker, the trajectory of a muon through the detector can be reconstructed. The charge of the muon is determined from the curvature of the reconstructed trajectory.

The muon spectrometer contains high precision tracking chambers, as well as separate trigger. The large barrel toroidal magnet provides the magnetic field needed for muon track bending in the $|\eta| < 1.0$ region. An end-cap magnet is inserted in each end of the large barrel toroid and provides the magnetic field in the $1.4 < |\eta| < 2.7$ region. In the transition region ($1.0 < |\eta| < 1.4$), the magnetic field is provided by a combination of the barrel and the end-cap fields.

The muon spectrometer can be split in the following parts: the muon chamber, monitored drift-tube chambers, cathode strip chambers, resistive plate chambers, and thin gap chambers. The location of these elements are shown in Figure 2.7.

2.2.4 Trigger and data acquisition system

The data production rate at LHC is very high, but often the events are of no interest. Therefore, a trigger system is used to quickly make decisions, in the "online environment", on whether the event should be kept or dropped.

The ATLAS trigger system is based on three levels of online event selection, where each level refines the decision made by the former level.

The level 1 trigger system must reduce the number of events starting from a bunch-crossing rate of 40 MHz to less than 75 MHz, based on measurements made with a reduced number of detectors.

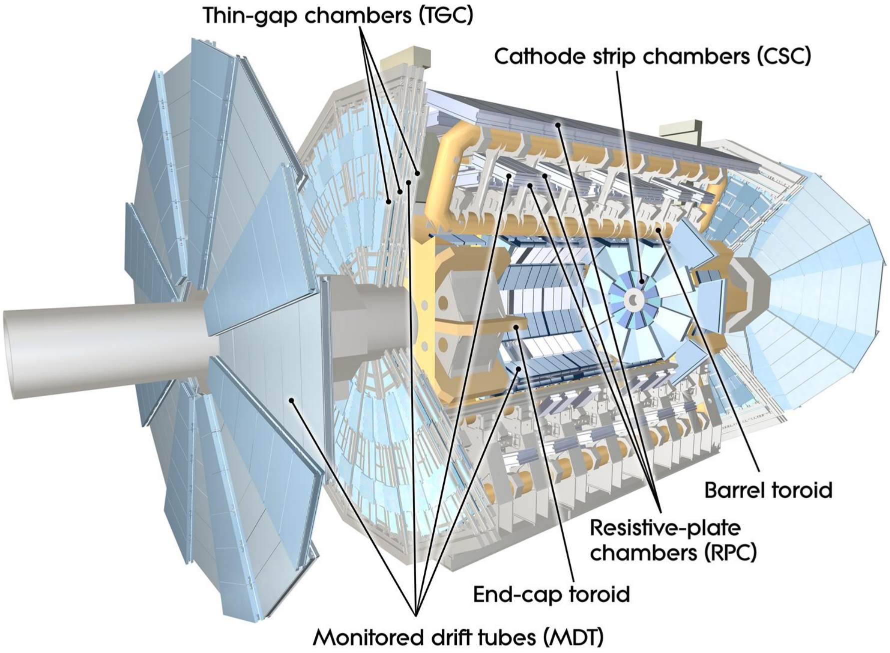

Figure 2.7: ATLAS muon spectrometer parts(ATLAS Experiment ©2011 CERN)

The level 2 trigger system reduces this further to approximately 1 kHz, and uses the "region of interest" data provided by the level 1 trigger. In order to make a decision, the level 2 trigger can, if needed, access the data provided by all the detectors.

The level 3 trigger reduces the output rate by ten times, down to approximately 100 Hz, using offline algorithms and methods adapted to the online environment.

A diagram showing the design of the trigger and data acquisition system is shown in Figure 2.8.

2.2.5 Event reconstruction

To illustrate how the signals received from various parts of the ATLAS detector are used to reconstruct an event, the reconstruction of a top dilepton event (See Figure 1.2) candidate is given as an example.

Given a top dilepton event, the top quarks cannot be detected directly, as each of them quickly decay to a W boson and a bottom quark.

As mentioned in Subsection 1.2.1, in the top dilepton channel the bottom quarks form two b-jets, while the W bosons decay to a charged lepton and a neutrino.

The neutrinos will escape undetected, while the charged lepton will leave a charged track in the tracking system. In order to measure the sign of a charged particle, the tracking system is placed inside a 2 T magnetic field. This way, the sign of the charge can be determined from the track curvature. Further information from the muon spectrometer helps to identify whether the lepton was an electron or a muon.

If the lepton is an electron or positron, the electromagnetic calorimeter registers energy deposition in a region coherent with the tracking system information. The hadron calorimeter should register little or no energy deposition.

If the lepton is a muon or an antimuon, it will leave almost no energy on both the electromagnetic and the hadron calorimeter, but the muon chambers should detect the presence of a particle that is coherent

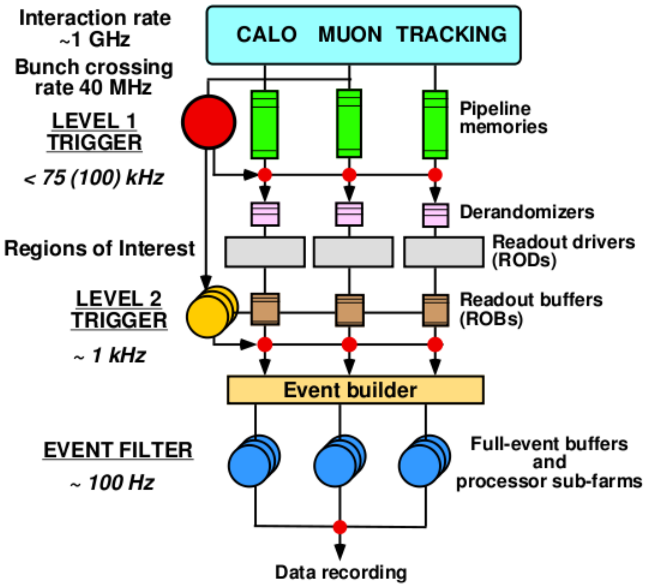

Figure 2.8: ATLAS trigger levels (taken from [1])

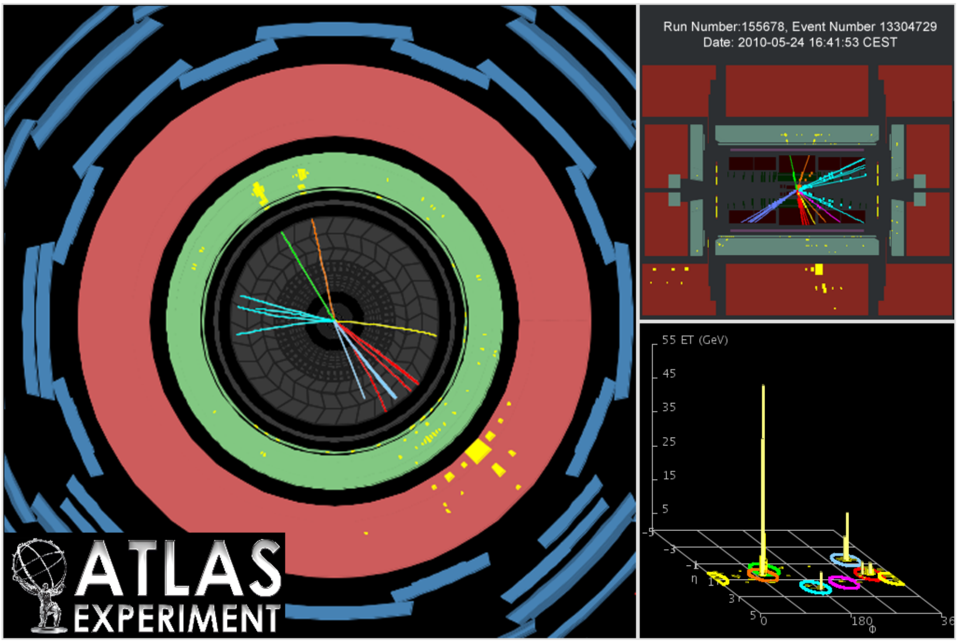

Figure 2.9: Event display of an ee channel dilepton event candidate [35]. (ATLAS Experiment ©2011 CERN)

with the tracking system information.

On the other hand, the bottom quarks hadronize. When hadronization happens, many particles are produced in a collimated way. Many of these particles also decay, forming more particles. Kinematic constraints give these particles a preferred direction, given by the momentum of the hadronizing parent particle. The group of all these particles is called a jet. If the track information on each particle produced were to be known with perfect precision, it would be possible to trace all the particles in a jet back to the particle that hadronized. But in practice the particle tracks precision is limited, and this limits our ability to reconstruct and identify jets. Instead, those showers are considered as one object. In order to identify the formation of jets, the anti-$\mathrm{k_t}$ jet reconstruction algorithm is used [10].

From the former discussion, one can expect a jet signature to be complicated: the tracking system would detect many particle tracks going towards a preferred direction, the electromagnetic calorimeter and the hadron calorimeter would register a significant amount of energy deposition, and the muon chambers might detect particles if muons are formed during the particle decays.

Figure 2.9 shows an event display for an ee channel dilepton event candidate. The electrons are shown by the green and orange track, on the upper half of the detector. In the electrons' direction, it can be seen that the energy deposition in the electromagnetic calorimeter (green area), and that there is no energy deposition in the hadron calorimeter (pink area). Also, notice on the lower half of the detector the jet structure formed by the red tracks, and the energy deposition in both the electromagnetic and hadron calorimeter.

Chapter 3

Methodology

3.1 Method description

The general description of the method followed to compute the top quark mass is described as the following series of steps:

- Find an observable which depends on the top quark mass
- Create a calibration curve from Monte-Carlo simulation samples with different top quark mass input
- Measure the chosen observable in data and obtain the top quark mass value from the calibration curve
- Consider the systematics effects that could modify the measurement

This thesis project uses the mean value of the m_{T2} distribution as the top quark mass dependent observable, which is to be measured in the dilepton channel. Additionally, a second observable is used, namely the mean value of the p_T^{leptons} distribution in the dilepton channel.

Additionally to the computation of the top quark mass measurement and the systematics effects, multivariable analysis is applied to minimize the systematic uncertainty. Furthermore, a second mass measurement is made using the variable p_T^{leptons} defined in Section 1.4 and merged with the measurement obtained using m_{T2}. This is done in order to reduce the jet energy scale uncertainty, which is the main source of uncertainty.

3.2 Main background

As mentioned in Subsection 1.2.1, the signature of the $\mathrm{t\bar{t}}$ dilepton channel produces:

- Two leptons (electrons or muons)
- Two jets (from the b-jets)
- missing transverse momentum (from the neutrinos)

Unfortunately, the dilepton channel is not the only decay channel that produces such a signature. This background comes mainly from the following processes [25]:

- Single top events
- Z+jets events

- Diboson events
- Fake leptons

The first three events produce a signature with two leptons (See Figure 3.1). Additional jets can be formed by gluon radiation. This could lead to a signature containing two leptons, and two or more jets. These events also contain missing transverse momentum, either through neutrino production 3.1a, 3.1c, through detector resolution, through detector mismeasurement, or through misreconstruction.

Events with fake leptons are events where a hadron is misidentified as a lepton. Therefore, an event with one lepton and jets could be reconstructed as an event with two leptons and jets. This could lead to the misidentification of a dilepton event.

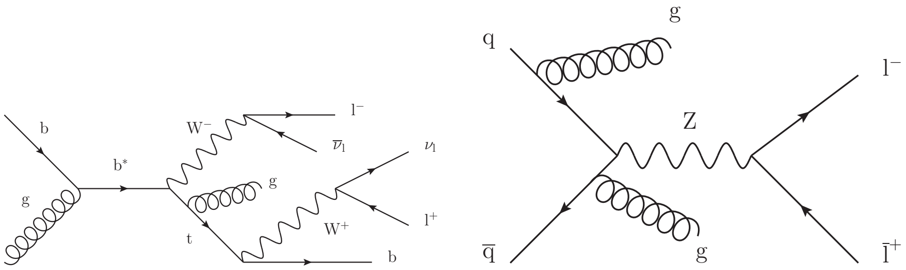

(a) Single top (b) Z+jets

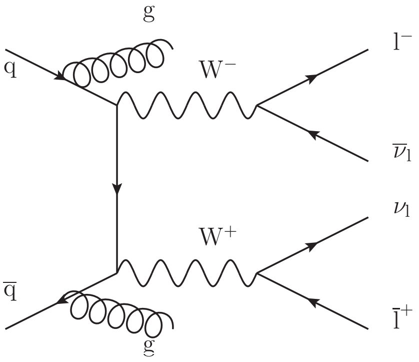

(c) Diboson

Figure 3.1: Examples of background proccesses

3.3 Event selection

In order to select dilepton events and reduce the background, the following selection cuts are applied [25]:

- There must be exactly two oppositely-charged leptons (ee, $\mu\mu$, eμ).
- Each electron must have a transverse momentum[1] of at least $p_T > 25$ GeV, and each muon must have at least $p_T > 20$ GeV

---

[1] Defined in appendix A

- There must be at least two jets with $p_T > 25$ GeV and pseudorapidity[2] $|\eta| < 2.5$.
- The leptons invariant mass[3] must satisfy $m_{ll} > 15$ GeV. This is used to reject the backgrounds coming from bottom quark production and vector-meson decays.
- For events in the ee and $\mu\mu$ channels:
  - $||\vec{p}_T^{\text{miss}}|| > 60$ GeV is required. This is used to reduce multijets background.
  - The leptons invariant mass must be outside of a 10 GeV window from the Z mass, i.e. $|m_{ll} - m_Z| > 10$ GeV ($m_Z = 91$ GeV). This is used to reduce the Z+jets events background.
- For events in the eμ channel:
  - The scalar sum of all selected leptons and jets energy[4] (H_T) must satisfy $H_T >$ 130 GeV. This is used to reduce the Z+jets events background for this channel.

3.4 m_{T2} computation

The straightforward way to compute m_{T2} given a set of values is to apply minimization by varying one invisible particle $\vec{p}_T$, and obtaining the second invisible particle $\vec{p}_T$ from Eq. 1.3.2. This proccess may take time, as it is a two dimensional scan on one of the invisible particle $\vec{p}_T$. Furthermore, the maximum of two m_T distributions is not always differentiable for every $\vec{p}_T$ value, and these non-differentiable points are located close to and at the minimum value. This means that derivative-based minimization algorithms like MIGRAD cannot be used. Therefore, the calculation must be performed using more computationally intensive algorithms, or using a different approach.

In this thesis, the m_{T2} variable is computed using the algorithm created by Cheng and Han [12]. This algorithm computes the m_{T2} value using a different approach. Instead of scanning on the invisible particle $\vec{p}_T$ two dimensional space, it tests values for m_{T2} directly.

The basic ideas behind the algorithm are shown below, and more detailed information can be found in [12].

- For a given m_{T2} test value, kinematic considerations restrict the possible value for each invisible particle. For each invisible particle, the allowed $\vec{p}_T$ value is constrained to an elliptical region on their respective $p_x p_y$ plane.

- These two elliptical regions are not independent, due to Eq. 1.3.2. Therefore, the two elliptical region can be put on the same $p_x p_y$ plane using Eq. 1.3.2 as transformation function.

- If all the kinematic considerations are to be satisfied, then the two allowed $\vec{p}_T$ elliptical regions must overlap.

- The area of the elliptical regions increase monotonically with the m_{T2} test input value. Therefore, the minimum is given by the m_{T2} value where the two elliptical regions start to overlap. This m_{T2} test value is equal to the final m_{T2} value.

---

[2] Defined in appendix A

[3] Defined in appendix A

[4] Defined in appendix A

3.4.1 m_{T2} computation in the dilepton channel

The m_{T2} computation algorithm created by Cheng and Han [12] demands the following input:

- The missing transverse momentum $\vec{p}_T^{\text{miss}}$.
- The energy and transverse momentum of the two visible particles.
- The mass of the invisible particle.

The value of the missing transverse momentum is obtained with the algorithm described in appendix A.

The energy and transverse momentum of the two visible particles are obtained according to Subsection 1.3.1, where the two highest p_T jets are selected as the jets produced by the bottom quarks.

The invisible particles in the top dilepton channel are neutrinos. In my analysis, I consider the neutrinos to be massless.

A problem arises when computing the value for the visible particle using Eq. 1.3.5: the lepton-jet pairing in a reconstructed dilepton event is not known a priori. To circumvent this problem, the m_{T2} value for both possible pairings is computed, and the pairing that returns the smallest m_{T2} value is taken.

3.5 Computer tools

During this study, mainly two computer tools were used: ROOT and MiLiTo.

3.5.1 ROOT

ROOT is an open-source object-oriented data analysis framework written in C++, and maintained by CERN [33]. As a data analysis framework, it is designed to help the physicist solve the data analysis challenges in high energy physics. Nowadays, ROOT can be considered the core program for data analysis in most CERN-related experiments.

ROOT provides a huge number of features and classes that makes data analysis an easier task. In particular, the following features are important to this study:

- Data reading and storage: data and Monte-Carlo samples are provided using ROOT files. ROOT files have several advantages including data storage and access optimization, file integrity checks (provided by the TFile class), corrupted files recovery (provided by the TFile class), and support for complex data structures (provided by the TTree class).
- Histogram analysis: ROOT is able to draw, edit, and analyse histograms in an easy and relatively clean way. It provides support for one, two, and three dimension histograms using the classes TH1, TH2, and TH3 respectively.
- Graph analysis: The ROOT class TGraphErrors provides tools that are useful for data points analysis. These tools include built-in data error management, which allows the user to set each data point with its respective uncertainty value. This is necessary in order to properly weight each data point during the fitting process. Like the histogram classes, the graph analysis classes also allow the user to draw, edit an analyse data in an easy way.

- Four-vector computing: The TLorentzVector class in ROOT provides very useful tools that covers practically most four-vector computations. These functions free the researcher from the burden of having to program all these operations by himself.
- Other analysis tools: ROOT provides many features. Some functions that deserves especial mention:
  - Mean value of a histogram distribution.
  - RMS of a histogram distribution.
  - Integral of a histogram distribution.
  - Correlation factor in a two dimensional histogram distribution.
  - Built-in n-degree polynomial fitter.
  - Histograms and graphs stacking.

The ROOT version used is 5.28.00.

3.5.2 MiLiTo

MiLiTo stands for MInimal Library for TOp studies. It is the main analysis software framework used in our group.

It implements the large amount of recommendations and corrections from the ATLAS top reconstruction group in a collective and organized way, in order to provide a common framework that takes care of these burdens at framework level. This allows the user-programmer to only deal with the problems that are specific to his/her own research.

MiLiTo is built on SFrame (available at http://sourceforge.net/projects/sframe/) , which is a C++ ROOT-based framework devoted to particle physics analysis, allowing the user to easily run analyses on a computing cluster.

MiLiTo provides built-in standard cutflows, including the standard cuts for dilepton channel discussed in Section 3.3. It also provides built-in functionality to evaluate systematic uncertainties, including the ones discussed in Chapter 4.

m_{T2} computation features were first included by Duc Bao Ta, and afterwards improved and adapted by me to use the m_{T2} computation algorithm created by Cheng and Han (See Section 3.4).

The MiLiTo version used is the release 16, revision 961.

3.6 Samples

3.6.1 Monte-Carlo samples

The samples used can be divided in four groups: $t\bar{t}$ samples, $t\bar{t}$ mass variation samples, background samples, and initial state radiation (ISR) and final state radiation (FSR) variation samples.

All $t\bar{t}$ samples without mass variation have a nominal input top quark mass of 172.5 GeV. The standard $t\bar{t}$ sample of this analysis is the sample no. 105200. The other central mass value samples are used to estimate systematic uncertainties. All central mass value samples used are listed in Table 3.1.

The $t\bar{t}$ mass variation samples are all generated with MC@NLO+HERWIG and are listed in Table 3.2.

The background samples are samples corresponding to other events that can be misreconstructed as dilepton events. They are listed in Table 3.3.

Input top quark mass (GeV) Sample Number	Generators	
172.5	105200	MC@NLO+HERWIG+JIMMY
172.5	105860	POWHEG+HERWIG+JIMMY
172.5	105861	POWHEG+PYTHIA+JIMMY
172.5	105205	ACER+PYTHIA

Table 3.1: Central mass value (172.5 GeV) $t\bar{t}$ Monte-Carlo samples

Input top quark mass (GeV)	Sample Number	Generators
140	117207	MC@NLO+HERWIG+JIMMY
150	117208	MC@NLO+HERWIG+JIMMY
160	106203	MC@NLO+HERWIG+JIMMY
165	106208	MC@NLO+HERWIG+JIMMY
167.5	106205	MC@NLO+HERWIG+JIMMY
170	106201	MC@NLO+HERWIG+JIMMY
175	106206	MC@NLO+HERWIG+JIMMY
177.5	106207	MC@NLO+HERWIG+JIMMY
180	106202	MC@NLO+HERWIG+JIMMY
190	106204	MC@NLO+HERWIG+JIMMY
200	117205	MC@NLO+HERWIG+JIMMY
210	117206	MC@NLO+HERWIG+JIMMY

Table 3.2: Mass variation $t\bar{t}$ Monte-Carlo samples

Background name	Sample Number	Generator
Single top	108340 - 108346	ALPGEN+JIMMY
Z+Jets ($Z^0 \to ee$)	107650 - 107655	ALPGEN+JIMMY
Z+Jets ($Z^0 \to \mu\mu$)	107660 - 107665	ALPGEN+JIMMY
Z+Jets ($Z^0 \to \tau\tau$)	107670 - 107675	ALPGEN+JIMMY
Z+bb ($Z^0 \to ee$)	109300 - 109303	ALPGEN+JIMMY
Z+bb ($Z^0 \to \mu\mu$)	109305 - 109308	ALPGEN+JIMMY
Z+bb ($Z^0 \to \tau\tau$)	109310 - 109313	ALPGEN+JIMMY
Diboson(ALPGEN)	107100 - 107111	ALPGEN+JIMMY
Diboson(HERWIG)	105985 - 105987	HERWIG
Drell-Yan (ee)	116250 - 116255	ALPGEN+JIMMY
Drell-Yan ($\mu\mu$)	116260 - 116265	ALPGEN+JIMMY
Drell-Yan ($\tau\tau$)	116270 - 116275	ALPGEN+JIMMY

Table 3.3: Background Monte-Carlo samples

The ISR and FSR variation samples are $t\bar{t}$ samples used to estimate the systematic uncertainty due to our limited knowledge in the modelling of ISR and FSR. All these variation samples use the same input events, but different ISR and FSR parameters in PYTHIA. They are listed in Table 3.4.

Name	Sample Number	Generator
Minimum ISR	117255	ACER+PYTHIA
Maximum ISR	117256	ACER+PYTHIA
Minimum FSR	117257	ACER+PYTHIA
Maximum FSR	117258	ACER+PYTHIA
Minimum ISR and FSR	117259	ACER+PYTHIA
Maximum ISR and FSR	117260	ACER+PYTHIA

Table 3.4: $t\bar{t}$ Monte-Carlo samples with modified initial state radiation and final state radiation

The Monte-Carlo sample production used is MC10b, although MC10a samples were used for preliminary analysis before the MC10b samples were available.

In order to compare with data, the Monte-Carlo samples luminosity is weighted down to the data luminosity.

3.6.2 Data samples

The data used come from proton-proton collisions at 7 TeV, measured by the ATLAS detector. In order to organize and separate different running time and conditions, the data samples are split in periods. The data from 2011 are split in 12 periods, corresponding to the letters: A, B, D, E, F, G, H, I, J, K, L, M.

This study uses 2011 data from period B2 until period K, giving a total integrated luminosity of 2.047 fb^{-1}. The details of these data samples are shown in Table 3.5.

Period	Date		Run number		Luminosity
	Start	Stop	Start	Stop	(pb^{-1})
B2	2011-Mar-22	2011-Mar-24	178044	178109	11.27
D	2011-Apr-14	2011-Apr-29	179710	180481	152.23
E	2011-Apr-30	2011-May-03	180614	180776	42.04
F	2011-May-15	2011-May-25	182013	182519	124.51
G	2011-May-27	2011-Jun-14	182726	183462	459.95
H	2011-Jun-16	2011-Jun-28	183544	184169	240.35
I	2011-Jul-13	2011-Jul-29	185353	186493	304.84
J	2011-Jul-30	2011-Aug-04	186516	186755	212.21
K	2011-Aug-04	2011-Aug-22	186873	187815	499.97
Total	2011-Mar-22	2011-Aug-22	178044	187815	2047.37

Table 3.5: Data samples used in this study

3.7 Computation of m_{T2} and p_T^{leptons} distributions from samples

MiLiTo is used to produce histogram files with the m_{T2} and p_T^{leptons} distributions from the different Monte-Carlo sample files. All histogram files from background samples (Table 3.3) are merged together into one total background (TotBg) histogram file. The TotBg histogram file is then merged with a $t\bar{t}$ histogram file to produce a final signal+background (sbg) histogram file.

For simplicity, the following terminology and notation will be used:

- Given the TotBg histogram, the histogram produced by merging it with the histogram produced from sample N, will be called the sbg(N) histogram.
- Unless explicitly stated as data histograms or data samples, the terms "sample" and "histogram" will refer to Monte-Carlo samples and the histograms obtained from those Monte-Carlo samples respectively.

3.8 Calibration curve and top quark mass value

The points in the calibration curve are obtained by extracting the value of an observable and its corresponding statistical error from twelve sbg histograms corresponding to the twelve mass variation samples (Table 3.2).

Then a second degree polynomial curve is fit to these points using ROOT, in order to obtain the calibration curve parameters. To obtain the top quark mass value, the quadratic formula is used as follows:

$$m_{top}(p_0, p_1, p_2, Y) = \frac{-p_1 \pm \sqrt{p_1^2 - 4p_2(p_0 - Y)}}{2p_2} \tag{3.8.1}$$

where each p_n is the calibration parameter corresponding to the $n - th$ degree term coefficient, and Y is the measured observable.

As an example, Figure 3.2 shows a calibration curve, which is obtained from the mass variation Monte-Carlo samples (See Table 3.2), associating the mean value of the m_{T2} distribution to the corresponding input top mass.

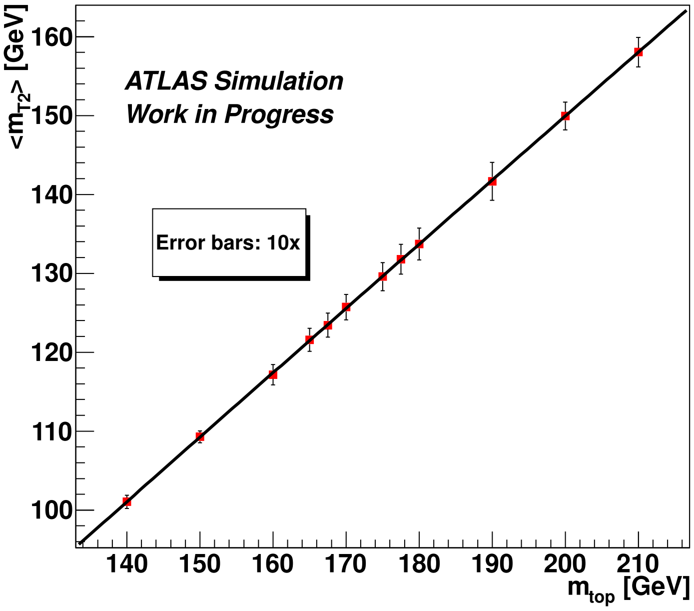

Figure 3.2: m_{T2} calibration curve at truth level

Chapter 4

Systematic uncertainties

To ensure proper treatment of the systematic uncertainties, the ATLAS collaboration provides some common tools. The estimation of my mass measurement systematic uncertainties is based on the ATLAS top reconstruction group's final recommendations for release 16 [37].

In order to determine the measurement's systematic uncertainty, the following sources of systematic uncertainties are considered.

- Systematic uncertainty from the fit of the calibration curve
- Objects[1] systematic uncertainties:
    - Jets
        - Jet energy scale
        - Jet energy scale additional pile-up uncertainty
        - b-jet energy scale
        - Jet reconstruction efficiency
        - Jet energy resolution
    - Muon
        - Muon trigger
        - Muon top-Id efficiency
        - Muon reconstruction efficiency
        - Muon momentum scale
        - Muon momentum resolution
    - Electrons
        - Electron trigger efficiency
        - Electron reconstruction efficiency
        - Electron identification
        - Electron energy scale
        - Electron energy resolution
    - Missing transverse momentum
        - CellOut and soft jet uncertainty

---

[1] Defined in appendix A

    - ∗ Pile-up uncertainty
    - ∗ Liquid argon problem

- Other systematic uncertainties:
  - Monte-Carlo generator systematic uncertainty
  - Parton shower and fragmentation model systematic uncertainty
  - Initial and final state radiation modelling systematic uncertainty

4.1 Systematic uncertainty from the fit of the calibration curve

The fit of the calibration curve is affected by insufficient statistics in the Monte-Carlo mass variation samples, and the use of a simplified fit model. In order to account for these systematic uncertainties, an uncertainty associated with the calibration point fit is introduced.

To estimate this uncertainty, error propagation is used (Eq. B.0.7). Replacing Eq. 3.8.1 in Eq. B.0.7, the uncertainty from the fit is given by:

$$\sigma^2_{m_{top}} = \sum_{i,j=0}^{2} \left[\frac{\partial m_{top}}{\partial p_i}\right]\left[\frac{\partial m_{top}}{\partial p_j}\right] V_{ij} \tag{4.1.1}$$

where λ has been replaced by m_{top}, given by Eq. 3.8.1, y_i has been replaced by the fit parameters, p_i, and V_{ij} is the covariance matrix of the fit parameters.

The fit parameters covariance matrix is supplied by ROOT. Although the partial derivatives can be computed analytically, in this study they are computed numerically, using:

$$\left[\frac{\partial m_{top}}{\partial p_i}\right] = \frac{m_{top}(p_i + \frac{\delta}{2}) - m_{top}(p_i - \frac{\delta}{2})}{\delta} \tag{4.1.2}$$

where $m_{top}(p_i + \epsilon)$ is the result of Eq. 3.8.1 with the i-th fit parameter modified by $+\epsilon$, while keeping the other fit parameters constant. The Y value is obtained from the sbg(105200) distribution.

4.2 Systematic uncertainties related to jets

4.2.1 Jet energy scale uncertainty (JES)

The jet energy scale (JES) systematic uncertainty accounts for the jet energy calibration, and is the dominant experimental uncertainty in this study.

To estimate the JES uncertainty, the jet energy is varied according to [17]. These recommendations are implemented using the JESUncertaintyProvider package, provided centrally by the ATLAS collaboration [37]. this package returns a scale factor based on the measured jet $\vec{p}_T$ and η values.

4.2.2 Jet energy scale additional pile-up uncertainty (JES pile-up)

The jet energy scale additional pile-up uncertainty (JES pile-up) accounts for the pile-up effects on the jet energy. The pile-up effects are caused by LHC high instantaneous luminosity, which leads to many proton-proton collisions almost at the same time. On average, there are 6 extra collisions additional to any signal processes during each bunch crossing in ATLAS [1]. This produce extra "pollution" in the event that affects the measured jet energy.

The JES pile-up uncertainty depends on the jet $\vec{p}_T$ and η values. The scale factors for this effect are provided centrally by the ATLAS collaboration [26] and given in Table 4.1.

p_T range (GeV)	$0 < \lvert\eta\rvert < 2.1$	$2.1 < \lvert\eta\rvert < 4.5$
20−50	0.05	0.07
50−100	0.02	0.03
> 100	0	0

Table 4.1: JES pile-up uncertainty scale factor dependence on the jet $\vec{p}_T$ and η values

4.2.3 b-jet energy scale uncertainty (bJES)

The b-jet energy scale (bJES) systematic uncertainty accounts from the uncertainties in the modelling of b-jets in the Monte-Carlo samples. It is only applied to jets that originate from a bottom quark at truth level. If a jet does not originate from a bottom quark at truth level, no bJES uncertainty is applied. The bJES scale factor depends on the b-jet p_T and are also provided centrally by the ATLAS collaboration [39]. These scale factors are presented in Table 4.2.

p_T range (GeV)	scale factor
20−40	0.025
40−80	0.020
80−210	0.017
210−600	0.011
> 600	0.0076

Table 4.2: bJES scale factor dependency on the b-jet p_T

4.2.4 JES, JES pile-up, and bJES systematic uncertainty estimation

The contribution of the JES uncertainty, the JES pile-up uncertainty, and the bJES uncertainty to the top quark mass measurement are computed simultaneously, where the scale factors of the JES, JES pile-up, and bJES systematic uncertainties are summed in quadrature and applied to the corresponding jets.

Three different distributions (sbg(105200)) are produced:

- The first distribution is produced with no rescaling and is used as control sample.
- The second distribution is produced by scaling down the jet energies in both the background and the $t\bar{t}$ samples.
- The third distribution is produced by scaling up the jet energies in both the background and the $t\bar{t}$ samples.

The observable value is measured from each sbg(105200) distribution and its corresponding mass value is computed from the calibration curve, producing three mass measurements.

The mass measurement from the second and the third sbg(105200) distributions are compared with the mass measurement from the first sbg(105200) distribution. Usually the results of these comparisons have opposite signs, and are taken as the positive and negative systematic uncertainty associated to JES, JES pile-up, and bJES.

In the unusual case that both results are positive (or negative), the strongest contribution is taken as the positive (or negative) systematic uncertainty, and the systematic uncertainty contribution on the negative (or positive) sign is taken as zero.

This systematic uncertainty contribution is generally asymmetric.

4.2.5 Jet reconstruction efficiency

The jet reconstruction efficiency (JRE) systematic uncertainty accounts for the effect of the limited efficiency of the used jet reconstruction algorithm. In this study, the jets are reconstructed using the anti-k_T algorithm. The efficiency of this reconstruction algorithm depends on the jet p_T and its η value.

In order to estimate the systematic uncertainty contribution of this effect, jets are randomly removed depending on the reconstruction efficiency corresponding to their given p_T and η values. This proccess is performed by MiLiTo using the package JetEfficiencyEstimator, provided centrally by the ATLAS collaboration [18].

In order to estimate the JRE contribution to the total systematic uncertainty, two sbg(105200) are created:

- The control sbg(105200) distribution is produced with no random jet removal.
- The modified sbg(105200) distribution is produced by removing jets randomly using the JetEfficiencyEstimator package on each event.

The observable value is measured from each sbg(105200) distribution and its corresponding mass value is computed from the calibration curve, producing two mass measurements. The difference between these two measurements is then symmetrized and used as the JRE systematic uncertainty estimate.

4.2.6 Jet energy resolution

The jet energy resolution (JER) addresses the experimental inability to perfectly measure the jet energy in ATLAS. In order to estimate the JER contribution to the total systematic uncertainty, the energy of each jet is smeared using a gaussian distributed random scale factor.

The smearing factor is computed by generating a gaussian distributed random number. The generating gaussian distribution mean is zero, and its standard deviation is one. This number is multiplied by a scale factor, which depends on the jet p_T and η. This scale factor is given by the JetEnergyResolutionProvider package, provided centrally by the ATLAS collaboration [19].

The algorithm to estimate the contribution to the total systematic uncertainty is analogous to the JRE systematic uncertainty estimation algorithm(Subsection 4.2.5).

4.3 Systematic uncertainties related to muons

4.3.1 Muon trigger efficiency

As the muon trigger has limited efficiency, a systematic uncertainty related to this limitation must be considered. In order to estimate this value, each event is reweighted according to its muon content. The reweighting scale factor is provided by the MuonSF package, produced by the ATLAS collaboration [34].

In order to estimate the systematic uncertainty, two modified sbg(105200) distributions are produced, corresponding to up-weighting and down-weighting.

The algorithm to estimate the contribution to the total systematic uncertainty is analogous to the JES systematic uncertainty estimation algorithm(Subsection 4.2.4).

4.3.2 Muon identification and reconstruction efficiency

The muon identification and reconstruction efficiency systematic uncertainty addresses our inability to perfectly identify and reconstruct muons.

The muon identification and reconstruction efficiency contributions to the total systematic uncertainty are estimated together, by reweighting each event twice: once for the muon reconstruction efficiency, and once for the muon identification efficiency.

The muon identification efficiency is provided by the same package used in the muon trigger efficiency systematic uncertainty estimation: MuonSF [37].

The muon reconstruction efficiency scale factor is provided by the MuonEfficiencyCorrections package [27], also provided by the ATLAS collaboration.

In order to estimate the systematic uncertainty, for each systematic uncertainty source, two modified sbg(105200) distributions are produced, corresponding to up-weighting and down-weighting.

The algorithm to estimate the contribution to the total systematic uncertainty is analogous to the JES systematic uncertainty estimation algorithm(Subsection 4.2.4).

4.3.3 Muon energy scale and energy resolution

The muon energy scale and energy resolution are correlated. They are both associated to the muons $\vec{p}_T$ value. The estimation of the systematic uncertainty from these effects is done by smearing the muons p_T. The smearing using the package MuonMomentumCorrections, provided by the ATLAS collaboration [28]. This package also provides the correlation matrix between the two components.

Contribution to the systematic uncertainty estimation

The muon energy scale and muon energy resolution correlation is taken care of by the MuonMomentumCorrections. In order to estimate the contribution to the total systematic uncertainty [28], four sbg(105200) are created corresponding to the smearing runs: MSUP, MSLOW, IDUP, IDLOW. The options MSUP and MSDOWN smear the measurement from the muon spectrometer, while IDUP and IDLOW smear the measurement from the inner detector.

The observable value is measured from each sbg(105200) distribution and its corresponding mass value is computed from the calibration curve, producing four mass measurements. The half-difference between the minimum and maximum mass value is symmetrized and taken as the estimated systematic uncertainty:

$$\sigma^2_{m_{top}} = \frac{m_{top}^{(MAX)} - m_{top}^{(MIN)}}{2} \tag{4.3.1}$$

where:

$$m_{top}^{(MAX)} = \max\left[m_{top}^{(MSUP)}, m_{top}^{(MSLOW)}, m_{top}^{(IDUP)}, m_{top}^{(IDLOW)}\right]$$
$$m_{top}^{(MIN)} = \min\left[m_{top}^{(MSUP)}, m_{top}^{(MSLOW)}, m_{top}^{(IDUP)}, m_{top}^{(IDLOW)}\right]$$

4.4 Systematic uncertainties related to electrons

4.4.1 Electron trigger efficiency, reconstruction efficiency, and identification uncertainty

The electron trigger efficiency, reconstruction efficiency, and the electron identification uncertainty are estimated using the same concept. Nevertheless, these uncertainties are considered uncorrelated and each of them are computed separately.

In order to estimate each contribution to the total systematic uncertainty, the events must be reweighted taking into account the electrons in the event.

This reweighting factor depends on the systematic contribution being evaluated, the number of electrons in the event, each electron's energy, η value, and the measuring calorimeter cells position.

In order to estimate the systematic uncertainty, for each systematic uncertainty source, two modified sbg(105200) distributions are produced, corresponding to up-weighting and down-weighting.

The algorithm to estimate the contribution to the total systematic uncertainty is analogous to the JES systematic uncertainty estimation algorithm(Subsection 4.2.4).

4.4.2 Electron energy scale and energy resolution

The electron energy scale and energy resolution systematic uncertainty address issues related to the electron energy measurement in ATLAS.

To estimate this systematic uncertainty, the energy of the electrons is scaled up or down. The scale factor depends on the systematic analysis type, the electron energy, and the η value. They are calculated with the EnergyRescaler package, provided by the ATLAS collaboration [37].

In order to estimate the systematic uncertainty, for each systematic uncertainty source, two modified sbg(105200) distributions are produced, corresponding to scaling up and scaling down.

The algorithm to estimate the contribution to the total systematic uncertainty is analogous to the JES systematic uncertainty estimation algorithm(Subsection 4.2.4).

4.5 Systematic uncertainties related to the missing transverse momentum

There are four systematic uncertainty sources related to $\vec{p}_T^{\text{miss}}$ [37]: the cell-out systematic uncertainty, the soft-jet systematic uncertainty, the pile-up systematic uncertainty for $\vec{p}_T^{\text{miss}}$, and the liquid argon hole problem systematic uncertainty. Except for the cell-out and soft-jet systematic uncertainties, which are computed together and are 100% correlated, all the other systematic uncertainties are taken as uncorrelated.

As pile-up also affects the $\vec{p}_T^{\text{miss}}$ computation, a systematic uncertainty related to this has also to be taken into account.

About the liquid argon hole problem [21]:

> On April 30th 2011, 6 of the front end boards (FEBs) we lost due to a problem with Controller Board in I15L. Unfortunately, this failure occurred after the production of the MC10 Monte Carlo and measures are required to fix this at the analysis level.

In terms of data samples, the 2011 data from period E to H are affected by this problem [14]. The effects of this fix is a source of systematic uncertainty, and is described in [21].

The TopMetTool package provided by the ATLAS collaboration is used to produce varied samples that accounts for each of the listed systematic uncertainties. In order to estimate the systematic uncertainty, this package rescales the $\vec{p}_T^{\text{miss}}$ value, either up-scaling or down-scaling it.

The algorithm to estimate the contribution to the total systematic uncertainty is analogous to the JES systematic uncertainty estimation algorithm(Subsection 4.2.4). It is applied separately on each block of systematic sources (i.e. cell-out and shoft-jet simultaneously, pile-up in one run, and liquid argon hole in another run).

4.6 Other systematic uncertainties

4.6.1 Initial and final state radiation

The systematic uncertainty associated with the initial state radiation (ISR) and the final state radiation (FSR) measures the impact of our limited knowledge on the modelling of these phenomena. Although the input values given to the Monte-Carlo generators that create the Monte-Carlo samples used are believed to be a good approximation to reality, but many assumptions and simplifications are made during the simulation. These assumptions and simplifications are sources of systematic uncertainties and have be addressed accordingly.

Dedicated samples have been created to account for this problem, namely the ISR/FSR variation samples (Table 3.4). In order to estimate the systematic uncertainty [37], 7 sbg distributions are produced:

- sbg(105205): control sbg distribution
- sbg(117255): Minimum ISR sbg distribution
- sbg(117256): Maximum ISR sbg distribution
- sbg(117257): Minimum FSR sbg distribution
- sbg(117258): Maximum FSR sbg distribution
- sbg(117259): Minimum ISR and FSR sbg distribution
- sbg(117260): Maximum ISR and FSR sbg distribution

The observable value is measured from each sbg distribution and its corresponding mass value is computed from the calibration curve. This amounts to a total of seven mass measurements.

The mass measurement from all distributions are compared (by subtraction) to the mass measurement from the control sbg distribution. The most positive deviation and the most negative deviation are considered, respectively, as the positive and negative systematic uncertainty. If all the deviations have the same sign, the systematic uncertainty of the opposite sign is zero.

4.6.2 Monte-Carlo generator

The Monte-Carlo generator MC@NLO(+HERWIG) is used to produce the standard $t\bar{t}$ sample in this study, as well as all mass variation samples. In order to account for the differences and a possible bias produced by choosing MC@NLO over another generator, a systematic uncertainty associated with the Monte-Carlo generator is introduced.

In order to estimate this systematic uncertainty [37], two sbg(105200) distributions are produced:

- The MC@NLO sample generated sbg distribution (i.e. the sbg(105200) distribution).
- The POWHEG sample generated sbg distribution (i.e. the sbg(105860) distribution).

Comparing the mass measurement calculated from the results of these two distributions estimates the effect of replacing the MC@NLO generator by POWHEG (keeping HERWIG constant). Therefore, the systematic uncertainty for the Monte-Carlo generator is estimated as:

$$\Delta m = \pm|m_{105200} - m_{105860}| \tag{4.6.1}$$

where Δm, m_{105200} and m_{105860} are the Monte-Carlo generator systematic uncertainty, the top masses measured from sbg(105200), and sbg(105860) respectively.

4.6.3 Parton shower and fragmentation model (Parton/Fragmentation)

HERWIG(+MC@NLO) is the second component in the production of the standard $t\bar{t}$ sample in this study, as well as all mass variation samples. HERWIG generates the decay and parton shower in the samples.

In order to account for the differences and a possible bias produced by choosing HERWIG over another modelling tool, a systematic uncertainty associated to the parton shower and fragmentation model is introduced.

The procedure to estimate this systematic uncertainty is completely analogue to the one used to estimate the Monte-Carlo generator contribution to the systematic uncertainty [37]. Two sbg(105200) distributions are produced:

- The HERWIG sample generated sbg distribution (i.e. the sbg(105260) distribution).
- The PYTHIA sample generated sbg distribution (i.e. the sbg(105261) distribution).

Comparing the mass measurement calculated from the results of these two distributions estimates the effect of replacing HERWIG by PYTHIA (keeping HERWIG constant) as decay and parton shower model.

The estimation of the systematic uncertainty is similar to the estimation of the Monte-Carlo generator systematic uncertainty, replacing sbg(105200) for sbg(105261).

4.6.4 Fake leptons

A fake lepton is an object that has been misreconstructed as a hard process lepton. Possible sources for fake leptons include photons, pions, hadron decays, misreconstructed jets, and others.

To estimate the fake leptons rate, the FakesMacros package provided by the ATLAS Collaboration is used [38]. The fakes estimation performed by this package uses the matrix method, which is described in detail in [6].

The package also provides systematic uncertainty estimation features. This is done by changing the normalization by 50 %, in order to account for mismeasurement of the fakes rate.

The algorithm to estimate the contribution to the total systematic uncertainty is analogous to the JES systematic uncertainty estimation algorithm(Subsection 4.2.4).

4.7 Optimization cuts

To reduce the effects of the systematic uncertainties described above, additional cuts are applied during the dilepton selection process.

In order to find a good set of cuts, multivariate analysis was used. The variables used in the analysis were: number of jets, leading lepton p_T, sub-leading lepton p_T, leading jet p_T, sub-leading jet p_T, $\vec{p}_T^{\,\text{miss}}$, and U_T.

The multivariate analysis consists of varying all the cuts in a systematic and ordered way. For each cut variation, the systematic uncertainty is estimated. The number of cuts tested in each analysis is given by:

$$N_{cuts} = \prod_{i=1}^{n} a_i$$

where N_{cuts} is the number of cuts tested, n is the number of variables taking place in the analysis, and a_i is the amount of different values that the i-th variable takes during the analysis.

The multivariate analysis was made in a series of steps. For the leptons and jets p_T cuts, the variation was performed from $p_T < 25$ to $p_T < 100$ in steps of 5 GeV. For the U_T cut, the variation was made from $p_T < 0$ to $p_T < 100$ in steps of 10 GeV. The m_{T2} variable was varied from 210 GeV to 300 GeV in steps of 10 GeV.

Based on this analysis, the following set of extra cuts was selected:

- Leading lepton p_T higher than 40 GeV.
- Sub-leading lepton p_T higher than 25 GeV.
- $U_T < 60$ GeV.
- $m_{T2} < 220$ GeV.

This set of cuts was chosen based not only in the value of the systematic uncertainty estimation, but also on the amount of events kept after the extra cuts, the goodness of the calibration curve fit, the estability of the systematic uncertainty to variations in the cuts, and the number of cuts.

To avoid biased results, the whole analysis was made based only on Monte-Carlo samples.

Chapter 5

Analysis and results

5.1 m_{T2} histograms at truth level

In order to check whether there is a dependency between the m_{T2} variable and the Monte-Carlo samples input top mass, some m_{T2} histograms were created using Monte-Carlo samples with different input top mass at truth level. Information at truth level means that it is obtained directly from the event generator, without applying any detector effect like detector efficiency, detector resolution, and so on. Therefore, the events have perfect reconstruction and measurement.

To produce these histograms, no cuts are applied at all, as they are not needed. Instead, the events are ensured to be a dilepton event at generator level.

In Figure 5.1, the m_{T2} histograms are shown. It can be seen that the m_{T2} value is being shifted to the right as the input top mass increases. Note that each distribution features a sharp cut-off at the value of the input top mass, confirming that it is indeed a lower boundary to the parent particle mass, as mentioned in Section 1.3.

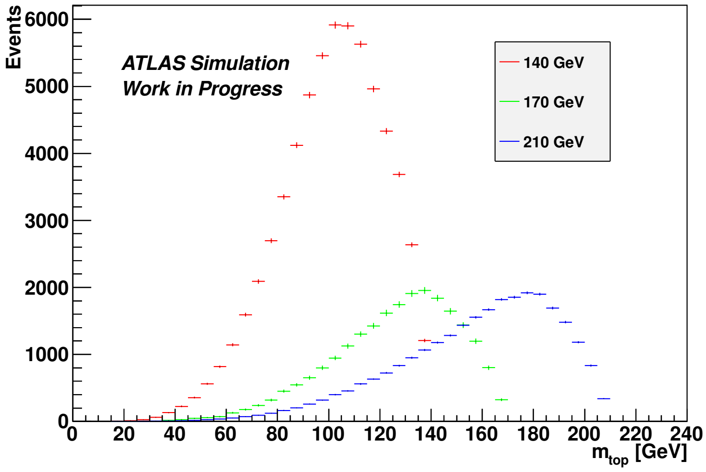

Figure 5.1: m_{T2} histograms with different input top mass at truth level

From the mass variation Monte-Carlo samples (See Table 3.2), a calibration curve can be created at truth level associating the mean value of the m_{T2} distribution to the corresponding input top mass, shown in Figure 3.2.

Although this calibration curve is not useful in practice, it shows that there is a dependency of our observable on the top mass, at least at truth level. This calibration curve has been fit with a second degree polynomial. From Figure 3.2, we see that the second degree polynomial fits the points extremely well. Also note that the error bars have been magnified 10 times in order to be seen.

5.2 Mass measurement using m_{T2}

In the previous section, the m_{T2} histograms at truth levels were shown. But in order to compare with the data, m_{T2} histograms at reconstruction level are needed. Information at reconstruction level means that the observables from each event are obtained after considering the possible detector effects that may alter the event's real values (truth value). These effects include event misreconstruction, detector efficiency and resolution, particle identification, detector parts that are known to be disabled or have lower quality, etc.

In order to produce these histograms, all the standard cuts (Section 3.3) and the optimization cuts (Section 4.7) are applied.

In Figure 5.2, these m_{T2} histograms are shown. It can still be seen that the m_{T2} value is shifted to the right as the input top mass increases, so the m_{T2} distribution depends on the input top mass at reconstruction level. Note that the sharp cut-off at the value of the input top mass is not present anymore, and a long tail is visible instead.

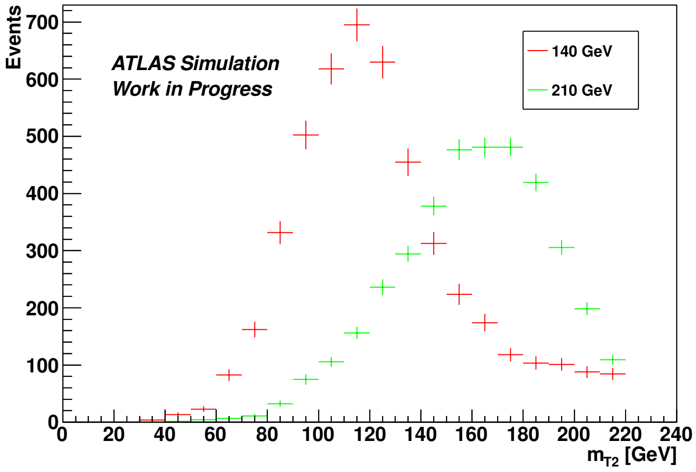

Figure 5.2: m_{T2} histograms with different input top mass at reconstruction level

As in truth level, a calibration curve can be created at reconstruction level associating the mean value of the m_{T2} distribution to the corresponding input top mass, as shown in Figure 5.3.

Parameter	Value	Error
p0	137.75	0.22
p1	0.4711	0.0082
p2	0.00088	0.00035

Table 5.1: m_{T2} calibration curve parameters

Again, the calibration curve is fitted with a second degree polynomial. The fit parameters are shown in Table 5.1 and the covariance matrix is:

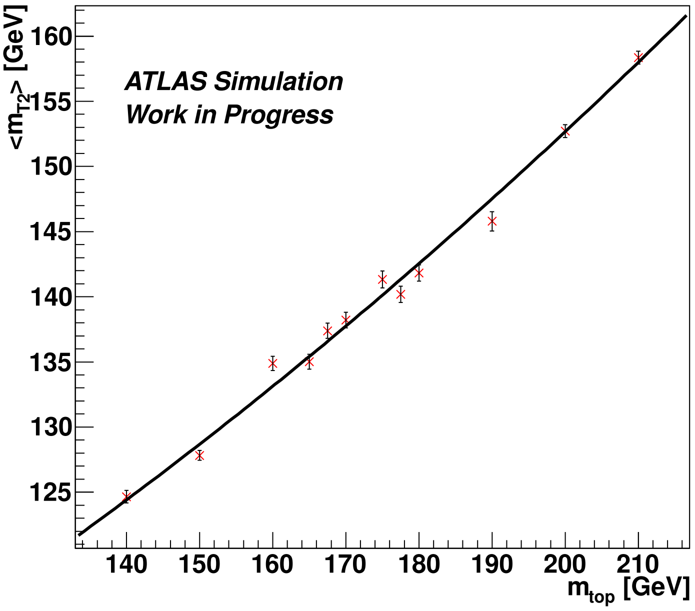

Figure 5.3: m_{T2} calibration curve at reconstruction level

$$V = \begin{pmatrix} 4.7\times10^{-02} & 4.7\times10^{-04} & -5.2\times10^{-05} \\ 4.7\times10^{-04} & 6.7\times10^{-05} & -1.2\times10^{-06} \\ -5.2\times10^{-05} & -1.2\times10^{-06} & 1.2\times10^{-07} \end{pmatrix} \tag{5.2.1}$$

It must be noted that in order to reduce the effects of the correlation between the parameters, the mass value is displaced by −170 GeV during calculations. That is:

$$m_{calibration} = m_{sample} - 170 \text{ GeV} \tag{5.2.2}$$

where $m_{calibration}$ is the mass input used to produce the calibration curve and m_{sample} is the nominal top mass input of each sample.

In order to obtain the mass, the inverse function is used:

$$m_{measured} = m_{fit} + 170 \text{ GeV} \tag{5.2.3}$$

where $m_{measured}$ is the value of the mass measurement, and m_{fit} is the mass value obtained by applying Eq. 3.8.1, with Y given in GeV.

To check for consistency between Monte-Carlo simulation and data, a plot comparing their m_{T2} distribution is shown in Figure 5.4. The Monte-Carlo samples assume a top mass value of 172.5 GeV.

From the m_{T2} distribution in data (shown in Figure 5.4), the observable is measured to be:

$$< m_{T2} >= 139.01 \pm 0.67 \text{ GeV} \tag{5.2.4}$$

Using the calibration curve fit, the top mass is computed to be:

$$m_{top} = 172.7 \pm 1.4 \text{ GeV} \tag{5.2.5}$$

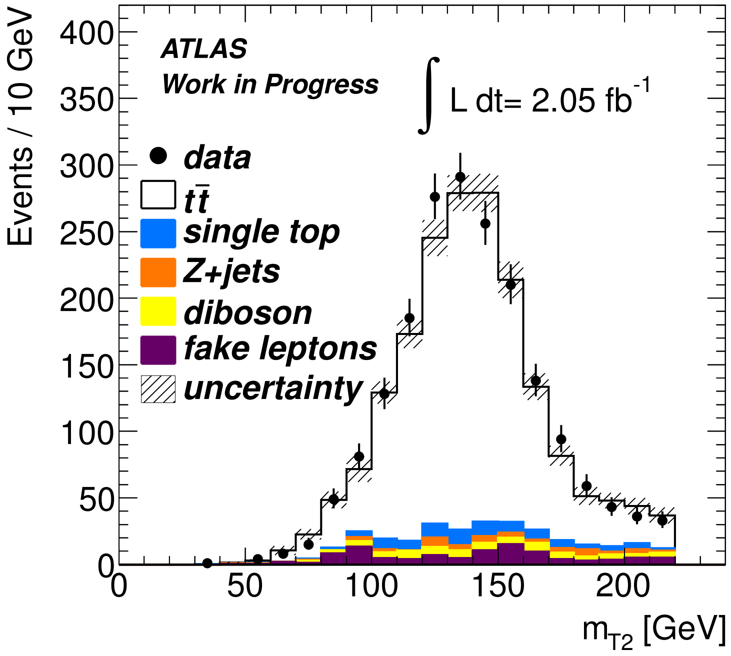

Figure 5.4: Comparison between Monte-Carlo and data m_{T2} distribution

where the uncertainty shown is the statistical uncertainty, which is obtained using Eq. B.0.7 with the information given in Eq. 5.2.1, Eq. 5.2.4, and Table 5.1.

5.3 Mass measurement using p_T^{leptons}

The mass measurement using p_T^{leptons} is analogous to the one using m_{T2}. First, a calibration curve is constructed using p_T^{leptons} distributions at reconstruction level. In order to produce these p_T^{leptons} distributions, only the standard cuts (Section 3.3) are applied. Figure 5.5 shows two of them.

By associating the mean value of the p_T^{leptons} distribution to the corresponding input top mass, the calibration curve for p_T^{leptons} is built. This is shown in Figure 5.6.

Parameter	Value	Error
p0	65.57	0.17
p1	0.1705	0.0060
p2	0.00084	0.00027

Table 5.2: p_T^{leptons} calibration curve parameters

The fit parameters for this calibration curve are shown in Table 5.2 and the covariance matrix has the value:

$$V = \begin{pmatrix} 2.9\times10^{-02} & 3.0\times10^{-04} & -3.2\times10^{-05} \\ 3.0\times10^{-04} & 3.6\times10^{-05} & -4.4\times10^{-07} \\ -3.2\times10^{-05} & -4.4\times10^{-07} & 7.0\times10^{-08} \end{pmatrix} \tag{5.3.1}$$

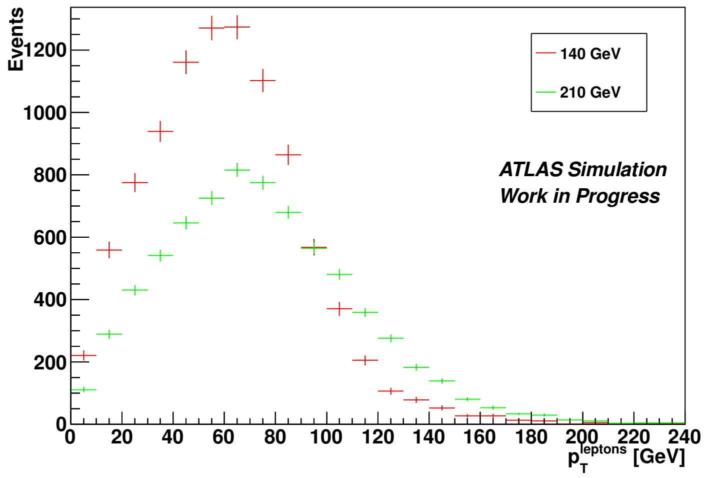

Figure 5.5: p_T^{leptons} distributions with different input top mass at reconstruction level

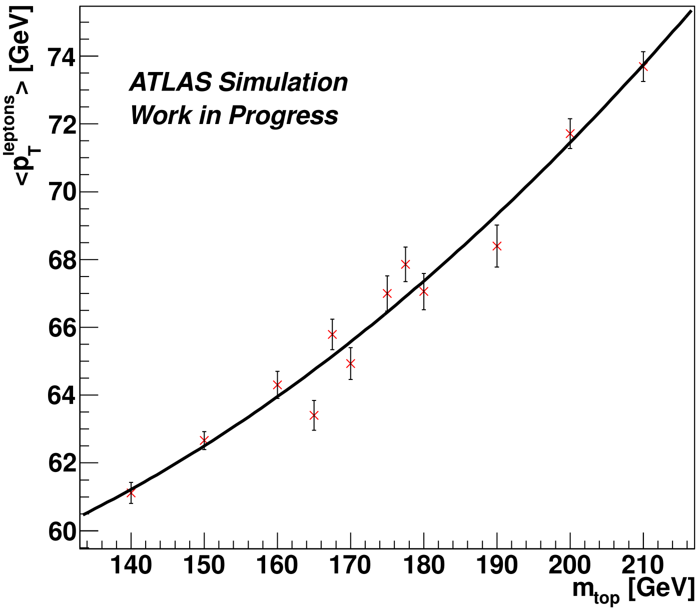

Figure 5.6: p_T^{leptons} calibration curve at reconstruction level

As in the measurement using m_{T2}, the mass value is displaced by -170 GeV during calculations in order to reduce the effects of the correlation between the parameters.

To check for consistency between Monte-Carlo simulation and data, a plot comparing their p_T^{leptons} distribution is shown in Figure 5.7. The Monte-Carlo samples have a input top mass of 172.5 GeV.

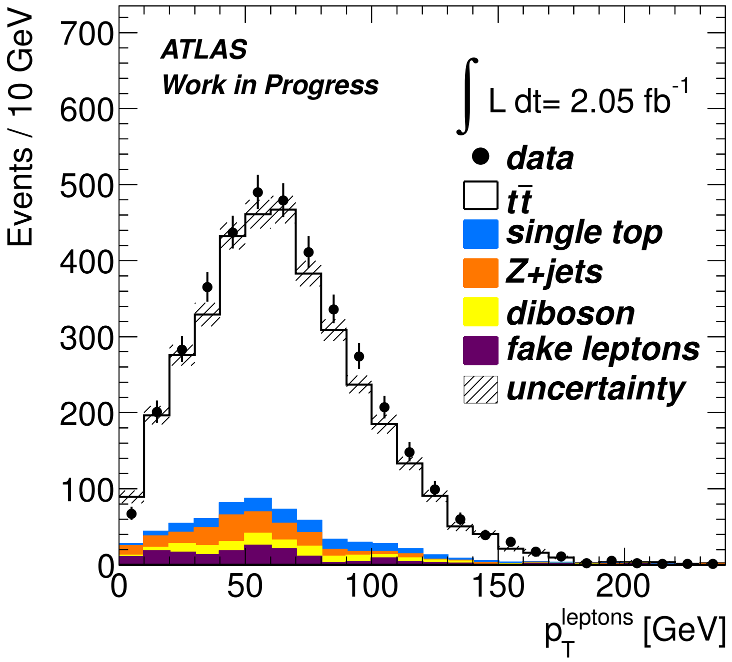

Figure 5.7: Comparison between Monte-Carlo and data p_T^{leptons} distributions

From the p_T^{leptons} distribution in data (Figure 5.7), the observable is measured to be:

$$< p_T^{\text{leptons}} >= 66.3 \pm 1.1 \text{ GeV} \tag{5.3.2}$$

Using the calibration curve fit, the top mass is found to be:

$$m_{top} = 174.1 \pm 3.0 \text{ GeV} \tag{5.3.3}$$

where the uncertainty shown is the statistical uncertainty, obtained using Eq. B.0.7 with Eq. 5.3.2, Eq. 5.3.1, and Table 5.2.

5.4 Measurement combination

In order to combine the top mass measurements obtained with m_{T2} and p_T^{leptons}, an algorithm is needed. This algorithm should take into account the statistical significance of each measurement, and the correlation between the two methods.

The measurement combination could have been done with a two dimensional fit. Instead, the method used to perform the measurement combination in this study is the least squares method[1]. This alternative was chosen due to its computational simplicity.

---

[1] See appendix B

In order to perform a combination with the least squares method, the correlation between the two measurements have to be determined. This is done by dividing the $t\bar{t}$ sample 105200 and all the background samples in 100 subsamples. Two mass measurements, one using m_{T2} and another one using p_T^{leptons}, are made on each subsample, and each mass measurement pair are registered.

The procedure described above produces 100 mass measurement pairs. These mass measurement pairs are plotted in Figure 5.8, and correlation analysis is applied to calculate the correlation coefficient between the two measurements.

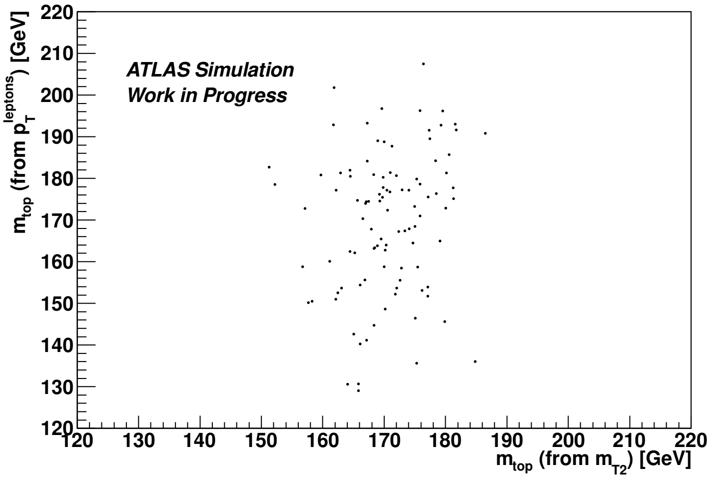

Figure 5.8: Correlation between the mass measurements using m_{T2} and p_T^{leptons}

The computation of the correlation coefficient is done by ROOT, giving the value:

$$\rho = 0.17 \tag{5.4.1}$$

Then, this value can be used to compute the weight given by Eq. B.0.6, obtaining:

$$w = 0.87 \tag{5.4.2}$$

where the measurement using m_{T2} is considered the first measurement, and the measurement using p_T^{leptons} is considered the second measurement, and σ_i is the statistical uncertainty of the i-th measurement.

Using Eq. 5.2.5, 5.3.3, and 5.4.2 on Eq. B.0.5, the combined top mass value is:

$$m_{top} = 172.9 \pm 1.2 \text{ GeV} \tag{5.4.3}$$

where the uncertainty shown is the statistical uncertainty, obtained using Eq. B.0.8.

5.5 Systematic uncertainty

To estimate the systematic uncertainty, the methodology described in Chapter 4 is used for the m_{T2}, the p_T^{leptons}, and the combined mass measurement.

The main sources of systematic uncertainty are shown in Table 5.3. The uncertainties coming from other sources were below 1 GeV and are presented in a separate table Table 5.5.

Description		Estimated systematic uncertainty (GeV)		
Name	Option	m_{T2}	p_T^{leptons}	Combined
JES, JES pile-up, and bJES	Down	−3.6	+2.2	−2.8
	Up	+3.6	−2.2	+2.8
Initial and final state radiation	ISR min.	−2.5	-3.1	−2.6
	ISR max.	+0.9	+1.5	+1.0
	FSR min.	+1.4	−0.60	+1.1
	FSR max.	−2.1	−1.8	−2.0
	ISR and FSR min.	−2.0	−3.0	−2.2
	ISR and FSR max.	−1.6	+0.25	−1.3
Monte-Carlo generator	—	±1.2	±0.42	±1.1
Parton/Fragmentation	—	±0.40	±1.4	±0.52
Fake leptons	Down	−0.12	+0.40	0.049
	Up	+0.71	+1.0	+0.74
Fit	—	±0.47	±1.0	±0.42

Table 5.3: Main contributions to the systematic uncertainty

From these tables, the total systematic uncertainty for each measurement can be computed by summing all uncorrelated systematic uncertainties in quadrature. The results are summarized in Table 5.4.

Name	Contribution to the total systematic uncertainty (GeV)					
	m_{T2}		p_T^{leptons}		Combined	
	Negative	Positive	Negative	Positive	Negative	Positive
JES, JES pile-up, and bJES	3.6	3.6	2.2	2.2	2.8	2.8
ISR and FSR	2.5	1.4	3.0	1.5	2.6	1.1
Monte-Carlo generator	1.2	1.2	0.4	0.4	1.1	1.1
Parton/Fragmentation	0.4	0.4	1.4	1.4	0.5	0.5
Fake leptons	0.1	0.7	0.0	1.0	0.0	0.7
Fit	0.5	0.5	1.0	1.0	0.4	0.4
Other uncertainties	0.2	0.2	0.6	0.5	0.2	0.3
Total	4.6	4.2	4.2	3.4	4.0	3.4

Table 5.4: Summary of systematic uncertainties

Description		Estimated systematic uncertainty (GeV)		
Name	Option	m_{T2}	p_T^{leptons}	Combined
JRE	—	$\pm 2.7 \times 10^{-2}$	$\pm 4.0 \times 10^{-2}$	$\pm 1.8 \times 10^{-2}$
JER	—	$\pm 1.3 \times 10^{-1}$	$\pm 4.5 \times 10^{-1}$	$\pm 1.7 \times 10^{-1}$
Muon trigger efficiency	Down	-5.0×10^{-2}	-1.4×10^{-2}	-4.5×10^{-2}
	Up	$+5.6 \times 10^{-3}$	$+2.0 \times 10^{-4}$	$+4.9 \times 10^{-3}$
Muon identification and reconstruction	Down	-2.1×10^{-3}	$+2.2 \times 10^{-3}$	-1.5×10^{-3}
	Up	$+2.1 \times 10^{-3}$	-2.2×10^{-3}	$+1.6 \times 10^{-3}$
Muon energy scale and energy resolution	MSLOW	-1.8×10^{-2}	-1.9×10^{-1}	-4.0×10^{-2}
	MSUP	-7.1×10^{-2}	$+4.7 \times 10^{-2}$	-5.6×10^{-2}
	IDLOW	$+2.4 \times 10^{-2}$	-2.3×10^{-1}	-8.8×10^{-3}
	IDUP	$+3.4 \times 10^{-2}$	$+1.8 \times 10^{-1}$	$+5.4 \times 10^{-2}$
Electron trigger efficiency	Down	$+3.3 \times 10^{-3}$	-2.0×10^{-3}	$+2.6 \times 10^{-3}$
	Up	-3.4×10^{-3}	$+2.0 \times 10^{-3}$	-2.7×10^{-3}
Electron reconstruction and identification efficiency	Down	$+1.9 \times 10^{-2}$	-1.1×10^{-1}	$+2.4 \times 10^{-3}$
	Up	-1.6×10^{-2}	$+1.0 \times 10^{-1}$	-6.7×10^{-4}
Electron energy scale	Down	-6.1×10^{-2}	-3.5×10^{-1}	-1.0×10^{-1}
	Up	$+1.9 \times 10^{-1}$	$+5.9 \times 10^{-1}$	$+2.4 \times 10^{-1}$
Cell-out and soft-jet effect on $\vec{p}_T^{\text{miss}}$	Down	$+2.2 \times 10^{-2}$	$+6.1 \times 10^{-2}$	$+2.7 \times 10^{-2}$
	Up	$+1.9 \times 10^{-2}$	-2.5×10^{-1}	-1.5×10^{-2}
Pile-up effect on $\vec{p}_T^{\text{miss}}$	Down	$+1.0 \times 10^{-2}$	$+7.6 \times 10^{-2}$	$+1.9 \times 10^{-2}$
	Up	$+5.6 \times 10^{-2}$	-2.3×10^{-1}	$+1.9 \times 10^{-2}$
Liquid argon hole jet cleaning effect on $\vec{p}_T^{\text{miss}}$	Down	-1.9×10^{-1}	-2.5×10^{-1}	-1.1×10^{-1}
	Up	-3.0×10^{-2}	-6.8×10^{-2}	-3.1×10^{-2}

Table 5.5: Other contributions to the systematic uncertainty

5.6 Measurement summary

Summarizing the results from this chapter, the mass measurement using m_{T2} gives:

$$m_{top} = 172.7 \pm 1.4^{+4.2}_{-4.6}\ \text{GeV} \tag{5.6.1}$$

while the mass measurement using p_T^{leptons} is:

$$m_{top} = 174.1 \pm 3.0^{+3.4}_{-4.2}\ \text{GeV} \tag{5.6.2}$$

Combining these two results, we obtain:

$$m_{top} = 172.9 \pm 1.2^{+3.4}_{-4.0}\ \text{GeV} \tag{5.6.3}$$

Chapter 6

Conclusions and outlook

This thesis study a method to measure the top quark mass in the dilepton channel using the m_{T2} variable with ATLAS data.

Applying this method on 2 fb^{-1} ATLAS data, a measurement of the top mass is made, giving a value of $172.7 \pm 1.4^{+4.2}_{-4.6}$ GeV. This measurement is dominated by the systematic uncertainty, with the jet energy scale systematic uncertainty giving the strongest contribution.

The jet energy scale systematic uncertainty is reduced by combining the mass measurement using m_{T2} with a mass measurement performed with p_T^{leptons}. An improvement in the value of the systematic uncertainty is achieved with this measurement combination, yielding a top quark mass value of

$$m_{top} = 172.9 \pm 1.2^{+3.4}_{-4.0}\ \mathrm{GeV}.$$

In order to further improve the quality of this measurement in the dilepton channel, many approaches are suggested. The two most promising improvements are to perform optimization on each dilepton mode separately, and the use of b-tagging.

Further suggestions include the use of stronger cuts that could help reduce the systematic uncertainty on the measurement. With the ATLAS detector having collected 5 fb^{-1} so far, using stronger cuts is a viable option that was not feasible during the analysis stage of this thesis. Lastly, the use and combination of mass measurements using other observables can improve the final measurement.

Appendix A

Basic concepts

ATLAS coordinate system

The ATLAS coordinate system is a right-handed coordinate system defined as follows:

- The origin is located at the interaction point.
- The X axis points towards the center of the LHC ring.
- The Y axis points upwards, i.e. against the direction of Earth's gravitational force.
- The Z axis is along the beam direction, in a direction consistent with a right-handed coordinate system.

Objects

An object is a particle or group of particles that is measured as one entity. The objects in this thesis are photons, electrons, muons, and jets.

Transverse momentum ($\vec{p}_T$)

In ATLAS, the transverse plane is the plane that is transverse to the beam, i.e. the XY plane. Therefore, the transverse momentum is defined as the momentum in the XY plane, i.e. disregarding the Z component of the momentum.

Missing transverse momentum ($\vec{p}_T^{\text{miss}}$)

Due to momentum conservation, the vectorial sum of all momenta of the objects taking place in an event should be zero. But due to limited resolution, mismeasurements, and particles escaping without being detected, the sum of the transverse momentum of all objects might be different from zero.

The missing transverse momentum is defined as the vectorial sum of the transverse momentum of all photons, electrons, and jets.

Transverse energy (E_T)

The transverse energy of an object is the energy computed taking the momentum along the beam direction as zero. That is:

$$E_T = \sqrt{m^2 + p_x^2 + p_y^2} \tag{A.0.1}$$

Pseudorapidity (η)

The pseudorapidity is a one to one relationship between the angle between a given direction and the beam, given by:

$$\eta = -\ln\left[\tan\frac{\theta}{2}\right] \tag{A.0.2}$$

The pseudorapidity has some advantages over the angle with respect to the beam (θ). For example, the difference between two pseudorapidities is invariant to boosts along the beam axis.

Leptons invariant mass (m_{ll})

The invariant mass of two leptons is given by:

$$m_{ll} = P^2 = \sqrt{E^2 - \vec{p}^2} \tag{A.0.3}$$

where P is the sum of the four-momenta of the two leptons, E is the energy, and $\vec{p}$ is the three dimensional momentum.

The scalar sum of all selected leptons and jets energy(H_T)

The scalar sum of all selected leptons and jets in a dilepton event candidate is defined as:

$$H_T = p_T^{(lep1)} + p_T^{(lep2)} + p_T^{(jet1)} + p_T^{(jet2)} \tag{A.0.4}$$

where $p_T^{(lep1)}$, $p_T^{(lep2)}$, $p_T^{(jet1)}$, and $p_T^{(jet2)}$ are the module of the transverse momentum of the first lepton, second lepton, leading jet, and sub-leading jet respectively.

Appendix B

Measurement combination

Two top mass measurements can be combined using the least squares method. The contents of this section is based on [13], and a more detailed discussion can be found there. Here, only the results for the particular case that concerns this thesis, (i.e. combining two measurements) will be given.

The least squares method is based in minimizing the following quantity:

$$\chi^2(\lambda) = \sum_{i,j=1}^{N} (y_i - \lambda)(V^{-1})_{ij}(y_j - \lambda) \tag{B.0.1}$$

where N is the number of measurements, y_i represents each measurement, λ is the value of the combined measurement, and V is the covariance matrix for the N measurements.

For two measurements($N = 2$), the covariance matrix has the form:

$$V = \begin{pmatrix} \sigma_1^2 & \rho\sigma_1\sigma_2 \\ \rho\sigma_1\sigma_2 & \sigma_2^2 \end{pmatrix} \tag{B.0.2}$$

where σ_1 and σ_2 are the standard deviations for the first and second measurement, and ρ is the correlation between the two measurements.

Inverting this matrix, we obtain:

$$V^{-1} = \frac{1}{1-\rho^2} \begin{pmatrix} \frac{1}{\sigma_1^2} & -\frac{\rho}{\sigma_1\sigma_2} \\ -\frac{\rho}{\sigma_1\sigma_2} & \frac{1}{\sigma_2^2} \end{pmatrix} \tag{B.0.3}$$

From Eq. B.0.1 and Eq. B.0.3, we obtain:

$$\chi^2(\lambda) = \frac{1}{1-\rho^2} \left[\frac{(y_1-\lambda)^2}{\sigma_1^2} + \frac{(y_2-\lambda)^2}{\sigma_2^2} - 2\frac{\rho(y_1-\lambda)(y_2-\lambda)}{\sigma_1\sigma_2} \right] \tag{B.0.4}$$

Deriving Eq. B.0.4 with respect to λ, and setting the result equal to zero, the critical value of λ is obtained:

$$\lambda = wy_1 + (1-w)y_2 \tag{B.0.5}$$

where:

$$w = \frac{\sigma_2^2 - \rho\sigma_1\sigma_2}{\sigma_1^2 + \sigma_2^2 - 2\rho\sigma_1\sigma_2} \tag{B.0.6}$$

In order to obtain the statistical uncertainty, it is only necessary to use error propagation:

$$\sigma_\lambda^2 = \sum_{i,j=1}^{N} \left[\frac{\partial\lambda}{\partial y_i}\right]\left[\frac{\partial\lambda}{\partial y_j}\right] V_{ij} \tag{B.0.7}$$

where the numerical values for the y_i are replaced after derivation.
Using Eq. B.0.5 and Eq. B.0.6 in Eq. B.0.7, an expression for the statistical uncertainty is obtained:

$$\sigma_\lambda^2 = \frac{(1-\rho^2)\sigma_1^2\sigma_2^2}{\sigma_1^2+\sigma_2^2-2\rho\sigma_1\sigma_2} \tag{B.0.8}$$

Bibliography

[1] *ATLAS detector and physics performance: Technical Design Report*. Technical Design Report ATLAS. Electronic version not available. Geneva: CERN, 1999.

[2] G. Aad et al. 'The ATLAS Experiment at the CERN Large Hadron Collider'. In: *JINST* 3 (2008), S08003. DOI: `10.1088/1748-0221/3/08/S08003`.

[3] T. Aaltonen et al. 'Measurement of the top quark mass in the dilepton channel using m_{T2} at CDF'. In: *Phys. Rev. D* 81 (3 2010), p. 031102. DOI: `10.1103/PhysRevD.81.031102`. URL: `http://link.aps.org/doi/10.1103/PhysRevD.81.031102`.

[4] K. Aamodt et al. 'The ALICE experiment at the CERN LHC'. In: *JINST* 3 (2008), S08002. DOI: `10.1088/1748-0221/3/08/S08002`.

[5] F. Abe et al. 'Observation of Top Quark Production in $\overline{p}p$ Collisions with the Collider Detector at Fermilab'. In: *Phys. Rev. Lett.* 74 (14 1995), pp. 2626–2631. DOI: `10.1103/PhysRevLett.74.2626`. URL: `http://link.aps.org/doi/10.1103/PhysRevLett.74.2626`.

[6] B Abi et al. *Mis-identified lepton backgrounds to top quark pair production for Moriond 2011 analysis*. Tech. rep. ATL-COM-PHYS-2011-144. Geneva: CERN, 2011.

[7] A. Augusto Alves et al. 'The LHCb Detector at the LHC'. In: *JINST* 3 (2008), S08005. DOI: `10.1088/1748-0221/3/08/S08005`.

[8] Alan Barr, Christopher Lester and P. Stephens. 'm(T2) : The Truth behind the glamour'. In: *J. Phys.* G29 (2003), pp. 2343–2363. DOI: `10.1088/0954-3899/29/10/304`. eprint: `hep-ph/0304226`.

[9] Oliver Sim Brüning et al. *LHC Design Report*. Geneva: CERN, 2004.

[10] Matteo Cacciari, Gavin P. Salam and Gregory Soyez. 'The Anti-k(t) jet clustering algorithm'. In: *JHEP* 0804 (2008), p. 063. DOI: `10.1088/1126-6708/2008/04/063`. eprint: `0802.1189`.

[11] Serguei Chatrchyan et al. 'Measurement of the $t\bar{t}$ production cross section and the top quark mass in the dilepton channel in pp collisions at $\sqrt{s}$ =7 TeV. oai:cds.cern.ch:1354581'. In: (2011).

[12] Hsin-Chia Cheng and Zhenyu Han. 'Minimal Kinematic Constraints and m(T2)'. In: *JHEP* 0812 (2008), p. 063. DOI: `10.1088/1126-6708/2008/12/063`. eprint: `0810.5178`.

[13] G. Cowan. *Statistical data analysis*. Oxford science publications. Clarendon Press, 1998. ISBN: 9780198501565. URL: `http://books.google.com/books?id=JhL2FiF3hO4C`.

[14] *Dealing with LAr hardware problems in Monte Carlo*. 2011. URL: `https://twiki.cern.ch/twiki/bin/viewauth/AtlasProtected/LArCleaningAndObjectQuality#Dealing_with_LAr_hardware_proble`.

[15] D. Griffiths. *Introduction to Elementary Particles*. New York, USA: John Wiley & Sons, 1987.

[16] K. Hagiwara et al. 'Review of Particle Physics'. In: *Physical Review D* 66 (2002), pp. 010001+. URL: `http://pdg.lbl.gov`.

[17] *Jet energy scale and its systematic uncertainty in proton-proton collisions at sqrt(s)=7 TeV in ATLAS 2010 data*. Tech. rep. ATLAS-CONF-2011-032. Geneva: CERN, 2011.

[18] *Jet reconstruction efficiency*. 2011. URL: `https://twiki.cern.ch/twiki/bin/viewauth/AtlasProtected/TopJetReconstructionEfficiency#Jet_reconstruction_efficiency`.

[19] *JetEnergyResolutionProvider*. 2011. URL: `https://twiki.cern.ch/twiki/bin/view/Main/JetEnergyResolutionProvider`.

[20] M. Kobayashi and T. Maskawa. 'CP-Violation in the Renormalizable Theory of Weak Interaction'. In: *Progress of Theoretical Physics* 49 (Feb. 1973), pp. 652–657. DOI: `10.1143/PTP.49.652`.

[21] *LAr Hole*. 2011. URL: `https://twiki.cern.ch/twiki/bin/viewauth/AtlasProtected/TopETmissLiaison_EPS#LAr_Hole`.

[22] C.G. Lester and D.J. Summers. 'Measuring masses of semiinvisibly decaying particles pair produced at hadron colliders'. In: *Phys.Lett.* B463 (1999), pp. 99–103. DOI: `10.1016/S0370-2693(99)00945-4`. eprint: `hep-ph/9906349`.

[23] *Measurement of the Top-Quark Mass using the Template Method in pp Collisions at root(s)=7 TeV with the ATLAS detector*. Tech. rep. ATLAS-CONF-2011-033. Geneva: CERN, 2011.

[24] *Measurement of the top quark mass from 2011 ATLAS data using the template method*. Tech. rep. ATLAS-CONF-2011-120. Geneva: CERN, 2011.

[25] *Measurement of the top quark pair production cross section in pp collisions at ?s = 7 TeV in dilepton final states with ATLAS*. Tech. rep. ATLAS-CONF-2011-100. Geneva: CERN, 2011.

[26] *MultijetJESUncertaintyProvider for Top*. 2011. URL: `https://twiki.cern.ch/twiki/bin/viewauth/AtlasProtected/MultijetJESUncertaintyProviderTop`.

[27] *Muon Monte-Carlo efficiency scale factors*. 2011. URL: `https://twiki.cern.ch/twiki/bin/viewauth/AtlasProtected/MCPAnalysisGuidelinesEPS2011#AnchorEfficiencies`.

[28] *Muon momentum scale offset and resolution smearing*. 2011. URL: `https://twiki.cern.ch/twiki/bin/viewauth/AtlasProtected/TopCommonScales#Muon_momentum_scale_offset_and_r`.

[29] Lynne H. Orr. 'Decay versus hadronization for top quarks produced in hadron colliders'. In: *Phys. Rev. D* 44 (1 1991), pp. 88–98. DOI: `10.1103/PhysRevD.44.88`. URL: `http://link.aps.org/doi/10.1103/PhysRevD.44.88`.

[30] D.H. Perkins. *Introduction to high energy physics*. Cambridge University Press, 2000. ISBN: 9780521621960. URL: `http://books.google.com/books?id=e63cNigcmOUC`.

[31] *Prospects for the Measurement of the Top-Quark Mass using the Template Method with early ATLAS Data*. Tech. rep. ATL-PHYS-PUB-2010-004. Geneva: CERN, 2010.

[32] Arnulf Quadt. 'Top quark physics at hadron colliders'. In: *Eur. Phys. J.* C48 (2006), pp. 835–1000. DOI: `10.1140/epjc/s2006-02631-6`. URL: `http://arxiv.org/abs/hep-ph/0507207`.

[33] *ROOT Users Guide 5.26*. CERN, 2009. URL: `http://root.cern.ch/drupal/content/users-guide`.

[34] *Scale Factors For Use in Rel 16 2011 analyses: EPS and beyond*. 2011. URL: `https://twiki.cern.ch/twiki/bin/viewauth/AtlasProtected/TopCommonScales`.

[35] *Search for top pair candidate events in ATLAS at sqrt(s)=7 TeV*. Tech. rep. ATLAS-CONF-2010-063. Geneva: CERN, 2010.

[36] Tevatron Electroweak Working Group, CDF and D0 Collaborations. ‘Combination of CDF and DO results on the mass of the top quark using up to 5.8˜fb-1 of data’. In: *ArXiv e-prints* (July 2011). eprint: `1107.5255`.

[37] *Top Systematic Uncertainties 2011 rel 16*. 2011. URL: `https://twiki.cern.ch/twiki/bin/viewauth/AtlasProtected/TopSystematicUncertainties2011rel16`.

[38] *TopFakesEPS2011*. 2011. URL: `https://twiki.cern.ch/twiki/bin/viewauth/AtlasProtected/TopFakesEPS2011`.

[39] *b-jets JES uncertainty*. 2011. URL: `https://twiki.cern.ch/twiki/bin/viewauth/AtlasProtected/TopJetLiaison#b_jets_JES_uncertainty`.

List of Figures

List of Tables

I hereby certify that the work presented here was accomplished by myself and without the use of illegitimate means or support, and that no sources and tools were used other than those cited.

Bonn, …………………… ……………………………
Date Signature